KTH Engineering Sciences

Uncertainties in the Top Quark Background From the Monte Carlo Generator in the 1 Jet Channel of the $H \to WW^* \to \ell\nu\ell\nu$ Analysis

Author:
Nabila Shaikh (890227-0522)
nabilas@kth.se

Department of Physics
Royal Institute of Technology (KTH)

Master of Science Thesis
Supervisor: Jonas Strandberg
Examiner: Bengt Lund-Jensen

September 8, 2014

TRITA-FYS 2014:59
ISSN 0280-316X
ISRN KTH/FYS/–14:59—SE

Abstract

In July 2012, CERN announced the discovery of the Higgs particle with a mass of 125 GeV. Both the ATLAS and CMS experiments at the LHC reported independently that they had found a Higgs-like particle. This discovery is the final piece needed for the completion of the Standard Model. This thesis presents the updated analysis of the Higgs boson decay mode $H \to WW^* \to \ell\nu\ell\nu$ done at ATLAS, using 20 fb^{-1} and 4.5 fb^{-1} of collected data at $\sqrt{s} = 8$ and 7 TeV respectively. The results of the updated analysis have yet to be published but the signal strength for a Higgs boson at mass $m_H = 125$ GeV, given by last year's analysis, is $\mu = 1.01 \pm 0.31$ at a signal significance of 3.8 standard deviations. The uncertainty includes both systematic and statistical components.

In this thesis the estimation of theoretical systematic uncertainties of the MC generators in the top background is presented. The generators that model the matrix elements and parton showers are analysed in the $N_{jet} = 1$ channel of the $H \to WW^* \to \ell\nu\ell\nu$ analysis.

Sammanfattning

I juli 2012 tillkännagav CERN att en Higgspartikel, med massan 125 GeV, hade upptäckts. Både CMS- och ATLAS-experimenten rapporterade oberoende av varandra att en Higgsliknande partikel hade hittats och med denna uptäckt är nu Standardmodellen fullbordad. Denna avhandling sammanfattar den uppdaterade Higgsanalysen gjord av ATLAS-gruppen för sönderfallskanalen $H \to WW^* \to \ell\nu\ell\nu$. Analysen har gjorts på den uppsamlade datamängden 20 fb^{-1} vid kollisionsenergin $\sqrt{s} = 8$ TeV och 4.5 fb^{-1} vid kollisionsenergin $\sqrt{s} = 7$ TeV. Resultaten från den uppdaterade analysen är dock ännu inte publicerad. Signalstyrkan från 2013 års analys av datan för en Higgsmassa på $m_H = 125$ GeV ges av $\mu = 1.01 \pm 0.31$. Osäkerheten inkluderar både statiska och systematiska fel och signalöverkottet vid denna massa motsvarar 3.8 standardavvikelser.

Denna avhandling innehåller även en uppskattning av teoretiska systematiska osäkerheter i Monte Carlo generatorer för topkvarkbakgrunden. De generatorer om undersöks är event-generatorn och hadroniserings-generatorn för event med en jet.

Contents

Chapter 1

Introduction

The Standard Model (SM) was developed during the latter part of the 20th century by a collaboration of scientists around the world. It is a successful theory that describes fundamental interactions mediated through the electromagnetic, the weak and the strong force. It describes the interactions between the fundamental particles and anti-particles. The SM do not however describe interactions via the gravitational force, which is several orders of magnitude weaker than the other three.

After the discovery of the top quark in 1995 at Fermilab [1, 2] and the tau neutrino in 2000 [3] the main focus has been on finding the Higgs boson, the last missing piece of the SM. The Higgs boson and the associated Higgs field is responsible for the mass of the fundamental particles. It is also important for unifying the weak and electromagnetic interactions at a higher energy scale.

In July 2012, the ATLAS and CMS experiments at CERN announced the discovery of the Higgs boson with a mass of around 125 GeV. Further analysis has been made on the new particle in order to determine its properties such as spin, electric charge and interactions with other particles.

1.1 Outline of the Thesis

This thesis will give a brief theoretical introduction of SM and the Higgs mechanism in chapter 2 and a short presentation of the LHC and the ATLAS detector in chapter 3. The Higgs phenomenology is presented in chapter 4. The main focus of this thesis, presented in the following two chapters, is the updated and optimized Higgs analysis by the ATLAS experiment for the $H \to WW^* \to \ell\nu\ell\nu$ channel in chapter 5, and the analysis of the theoretical systematic errors in the top background for $N_{jet} = 1$ for the matrix element and parton shower in chaper 6. Lastly, the conclusions of the thesis are contained in chapter 7.

Chapter 2

The Standard Model

The Standard Model, SM, of particle physics describes how the fundamental particles interact with each other through the strong, weak and electromagnetic forces, excluding gravity that is still being best described by the general theory of relativity today. The SM is a so called quantum field theory, where particles are treated as excitations of different fields in nature. It is a theory with symmetries of the unitary product group $SU(3) \times SU(2) \times U(1)$.

The development of quantum field theories began with Paul Dirac and the quantization of the electromagnetic field in 1927 [4]. It was further developed by incoporating Albert Einstein's theory of special relativity in the quantum theory, which in the end created quantum field theory. Over the years quantum field theory was being perfected but one problem still remained: the infinities that entered the pertubative calculations. This was solved in the 1930s and 1940s by several physicists; Ernst Stueckelberg, Hans Bethe, Sin-Itiro Tomonaga, Julian Schwinger, Richard Feynman and Freeman Dyson through the process called renormalization. In 1954, Chen-Ning Yang and Robert Mills introduced non-abelian gauge theories in order to model the strong interaction. This was then also used to describe the weak interaction. In 1971, Gerard T'Hooft and Martinus Veltman published a paper showing that these type of gauge theories are renormalizable [5].

The idea of unifying the electromagnetic and weak interactions was already being pursued in the 1950s, and in 1957 Schwinger published an article proposing this idea [6]. His student, Sheldon Glashow, then developed this model further [7]. In 1967 Steven Weinberg and Abdus Salam incorporated the Higgs mechanism into Glashow's electroweak theory, and the extended theory was then called GWS theory. The Higgs mechanism, that was able to to explain the mass of the weak gauge bosons, was put forward in 1964 by three independent groups of physicists. François Englert and Robert Brout published a paper in August wherein they explained how the gauge bosons of weak interaction could acquire mass [8]. Peter Higgs published two papers the two following months on the same topic [9, 10]. Gerald Guralnik, Carl R Hagen and Tom Kibble also presented the mechanism in their paper published in November the same year [11]. A few years after, 'tHooft showed that theories with massive bosons can be renormalizable [12].

In this chapter, which is mainly based on Griffith' s book on the SM [13], we will review the particles that are in the SM and the different interactions between them.

2.1 Particles of the Standard Model

The SM contains a total of 25 particles and their corresponding antiparticles. Regular matter consists of fermions, spin-1/2 particles, while the particles that mediate the three forces (strong, weak and electromagnetic) and the Higgs boson are integer-spin particles called bosons. The fermions can further be divided into quarks, that carries color charge, and leptons, that do not. The quarks make up the composite particles called hadrons. Hadrons containing three quarks are named baryons while hadrons contining a quark and an antiquark are named mesons. The protons and neutrons that make up most of the matter in the universe are baryons while pions are the lightest mesons. The fermions follow Pauli-Dirac spin statistics meaning that they are subjugated to Pauli's exclusion principle [13]. The particles of the SM are given in the Tab. 2.1 with their respective masses[1], charge and spin. (The antiparticles have the same mass but different electric charge than their respective particle and are not shown in the table.)

2.1.1 Nature and Symmetries

Nature possesses many symmetries that are apparent in the formulations of our theories. Symmetries in physics corresponds to invariance of equations under some transformation. For example, the laws of physics are invariant under time translations, they are symmetric in time. Mathematically, symmetry operations are described by groups, and as previously mentioned the Lagrangian for the SM is invariant under the group $SU(3) \times SU(2) \times U(1)$, which is a group of gauge transformations. Both in classical and modern physics symmetries corresponds to conservation laws. For every symmetry there is a quantity that is preserved. The quantity that is conserved due to the invariance under time translations is energy. Gauge invariance corresponds to conservation of charge, e.g. electric charge in electromagnetism and color charge in strong interaction.

There are some other symmetries that are interesting as well; parity, charge conjugation and time reversal. Parity transformation, P, changes the sign of the spatial coordinates. Charge conjugation, C, changes the sign of the electric charge and time reversal, T, changes the direction of time flow. None of these symmetries are exact symmetries of the SM, meaning that the SM does not obey these symmetries separately, but the combined transformation CPT is an symmetry of the SM.

$$\begin{cases} P : \mathbf{r} \to -\mathbf{r} \\ C : 1 \to -1 \\ T : t \to -t \end{cases}$$

2.2 Interactions of the Standard Model

This section will give a short presentation to the three interctions described by the SM. An interaction, also known as a fundamental force, is a process in which elementary particles interact with each other.

[1]Since natural units ($c = \hbar = 1$) are used in this paper, the mass is given in units of energy.

Type	Particle	Electric charge (e)	Spin	Mass
Quark	u	$\frac{2}{3}$	$\frac{1}{2}$	2.3 MeV
	d	$-\frac{1}{3}$	$\frac{1}{2}$	4.8 MeV
	c	$\frac{2}{3}$	$\frac{1}{2}$	1.275 GeV
	s	$-\frac{1}{3}$	$\frac{1}{2}$	95 MeV
	t	$\frac{2}{3}$	$\frac{1}{2}$	173.07 GeV
	b	$-\frac{1}{3}$	$\frac{1}{2}$	4.18 GeV
Lepton	e	-1	$\frac{1}{2}$	0.511 MeV
	ν_e	0	$\frac{1}{2}$	< 2.05 eV
	μ	-1	$\frac{1}{2}$	105.66 MeV
	ν_μ	0	$\frac{1}{2}$	< 0.17 MeV
	τ	-1	$\frac{1}{2}$	1.78 GeV
	ν_τ	0	$\frac{1}{2}$	< 18.2 MeV
Boson	γ	0	1	0
	g	0	1	0
	Z	0	1	91.1876 GeV
	W^+	$+1$	1	80.385 GeV
	W^-	-1	1	80.385 GeV
	H	0	0	125.9 GeV

Table 2.1: Table of the particles of the Standard Model with their mass, electric charge (in units of elemtary charge) and spin (in units of $\hbar$). The different particles also have a corresponding antiparticle with opposite charge but the same mass and spin. The neutrinos are massless in the SM but experiments have shown that they do in fact have small masses. The values are taken from the Particle Data group [14].

2.2.1 Electromagnetism

The electromagnetic interaction is the most familiar interaction among the three described by the SM. It is an interaction between all electrically charged particles and is responsible for keeping the negatively charged electrons bound to the positively charged nucleus in atoms. Its massless mediator is the photon.

2.2.2 Strong Interaction

The strong interaction, mediated by the 8 different massless gluons, describes interactions between quarks and gluons. This interaction is described by quantum chromodynamics, QCD, and the symmetry for this theory is SU(3). Instead of electrical charge this interaction couples to color denoted, red, green and blue. The colors are conserved in all interactions. Two noteworthy characteristics of the strong interaction are confinement and asymptotic freedom. Confiment means that we will never find free quarks in nature, they will always appear in pairs of quark and antiquark, as mesons, or in triplets of quarks or triplets of antiquarks, as baryons. Asymptotic freedom comes from the fact that the strong force becomes weaker as the distance between the quarks decreases, the coupling constant is not actually constant but a function of energy. This is not a unique property of the strong interaction, the coupling constants of the electromagnetic and the weak interaction are also a functions of energy. However, while the strong coupling constant decreases in strength as the distance decreases, the electromagnetic and weak coupling constants increase in strength when the distance decreases.

2.2.3 The Weak Interaction

The weak interaction is the only interaction that can change particle flavors, e.g. turn a d-quark to a u-quark, and it is responsible for the familiar radioactive decay. It is mediated by the three massive gauge bosons, the Z boson and the $W^{\pm}$ bosons. The flavor changing interactions are mediated by the $W^{\pm}$ bosons and is called the charged currents. The interactions mediated by the Z boson conserve flavor and is called neutral currents.

Due to the gauge bosons' massive nature, the weak force is a short range interaction and hence the name weak interaction has been given to it. The weak interaction is also the only interaction in the SM that violates P-symmetry (it also violates CP symmetry). The reason for this violation is that the charged weak interaction only couples to so called left-handed chirality states. Chirality is a property of particles that is related to helicity, the scalar product between a particle's spin $\mathbf{s}$ and its momentum $\mathbf{p}$. For massless particles chirality and helicity coincide. The charged weak interaction couples only to left-handed chirality states (not left-handed helicity states).

The fermions can be divided into generations of particles with two doublet pairs of particles in each generation, shown in Tab. 2.2. For leptons, the charged currents only couples within each generation, the possible reactions are

$$l^- \rightarrow \nu_l + W^-$$

Type	First generation	Second generation	Third generation
Leptons	$\binom{\nu_e}{e}$	$\binom{\nu_\mu}{\mu}$	$\binom{\nu_\tau}{\tau}$
Quarks	$\binom{u}{d}$	$\binom{c}{s}$	$\binom{t}{b}$

Table 2.2: The elementary particles can be devided into three generations that contains particle pairs. The particles become more massive for the higher generations. This causes the particles of the higher generations to decay to the lower ones.

plus permutations where $l = e, \mu, \tau$. The coupling for the quarks, however, is not as simple. Even though the quarks can be divided into the three generations, the charged weak interactions couples across generations. The reason for this cross-generation couplings is that the physical states of the quarks, e.g. d, s etc., are not the eigenstates of the weak interaction. This leads to quark mixing and is given by the Cabibbo–Kobayashi–Maskawa matrix (CKM matrix) [15, 16]. Quark mixing enables the heavier quarks to decay into the lighter ones making the heavier quarks unstable and the lightest, d, u, stable. This is the reason for the abundance of protons (uud) and neutrons (udd) in the universe.

Mixing also occurs in the lepton sector. Neutrino oscillations, meaning that one neutrino can change into another, e.g. ν_μ changing into ν_e, has been confirmed by experiments [17]. This is possible if the neutrinos are in fact massive and if the mass states are not eigenstates of flavor of the weak force. (that are relevant for weak interaction). The neutrino mixing is given by a matrix called the Pontecorvo–Maki–Nakagawa–Sakata matrix (PMNS matrix) [18].

2.3 Feynman Calculus

In order to calculate decay rates and cross sections, the transition amplitude is needed. The transition amplitude is a function of the momenta that contains the dynamics of the proccess. To get the transition amplitude one must calculate complicated integrals that contain many variables. These integrals can be calculated by using pertubation theory. A graphical way to calculate the different terms in the pertubation theory was developed by Richard Feynman. A Feynman diagram is a pictorial description of a term in the pertubation series for a process. From the diagram one can write down the mathematical expression for the corresponding term and by adding several contributions from different Feynman diagrams the transition amplitude can be well approximated. An example of a Feynman diagram is given in Fig. 2.1.

For a pertubation theory to work, the terms in the series must become smaller and smaller for higher orders, it must converge towards the actual value. What physicists discovered was that many contributions (Feynman diagrams) to the transition amplitude that contains loops (higher order terms) are in fact infinite. This posed a big problem since the higher order terms need to get smaller and smaller, not infinte. A solution to this problem of infinite contributions was attained in the 1930s and 1940s and is called renormalization. Renormalization of a theory eliminates the infinite contributions

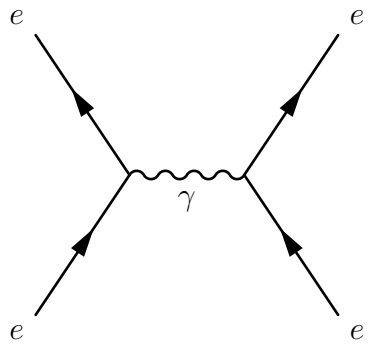

Figure 2.1: An example of a Feynman diagram. In this case an electron and positron annihilates into a virtual photon. The photon then produces a electron-positron pair.

by reparameterizing quantities like electric charge and mass [13]. For a field theory to successfully model the interactions of particles in nature it must be renormalizable.

2.4 The Electroweak Unification

In the SM, the electromagnetic and weak interactions have successfully been unified into one single interaction at very high energy scales. The electromagnetic and weak interactions seem at first to be very different and the possiblity to unify them might not be obvious. A way to unify them is to let the weak vector bosons become extremely massive [13]. This was accomplished by applying the BEH mechanism. This mechanism also gives rise to massive fermions. Initially, all gauge bosons in the SM are massless and the reason being gauge invariance. The gauge mass terms in the lagrangian are not invariant under gauge transformations and therefore cannot be present. Ignoring gauge invariance and introducing mass terms for the gauge bosons in the lagrangian will yield a non-renormalizable theory. The BEH mechanism manage to maintain the gauge invariance and successfully create massive gauge bosons while keeping the theory renormalizable.

The unification of the electromagnetic and weak interaction also predicted a weak neutral current that had not been observed at the time. This neutral current, mediated by the Z boson, was first experimentally confirmed in 1973 [19] and the discovery strengthened the support for the electroweak theory. The unification was first proposed in order to solve the problem of infinite contributions to reactions with more than one intermediate W boson. Those higher order contributions are supposed to be small, but were actually infinte. By unifying the electromagnetic and weak interaction, the contributions from the neutral current diagrams cancelled the infinite contributions (feynman diagrams), and an finite cross section, that agreed with experiments, was obtained.

The electroweak theory is, as mentioned before, a local gauge theory. The group asociated with this theory is the $SU(2) \times U(1)$ gauge group. Breaking the local symmetry of the $SU(2)$ group by introducing a scalar field will yield a theory with no massless gauge boson. This is not what we want since we do have a massless gauge boson, the photon. In order to keep one gauge boson massless and make the other three massive, an additional $U(1)$ symmetry is introduced. As previously mentioned, Feynman calculus is a pertubation theory where one pertubate around the ground state, also called the vaccum state. A symmetry of a theory is broken if the symmetry is not visible at first glance. When a

symmerty is broken, the lagrangian is still invariant but the ground state does not share this symmetry. It does not share this symmetry because there are several ground states and one has to be chosen when using Feynman calculus. When doing so, the symmetry is not apparent any more. If a continuous symmetry is broken then there exists an infinite number of ground states to choose from. The $SU(2) \times U(1)$ is a continous symmetry and there are infinite amount of different ground states to choose from.

When a continous symmetry is spontaneously broken a massless boson, called Goldstone boson, appear in the models for every symmetry that is broken [20]. For the electroweak interaction, the symmetry breakning via the BEH mechanism produces three Goldstone bosons. These bosons cause a problem since they are not found in the universe. Fortunately the solution to this problem exists. Because our theory respects gauge invariane, a gauge transformation can be applied without changing the physics. By choosing the right gauge one can turn these Goldstone bosons into the longitudinal polarizations of the massive vector bosons (only massive particles can have longitudinal polarizations) that are needed when they acquire mass.

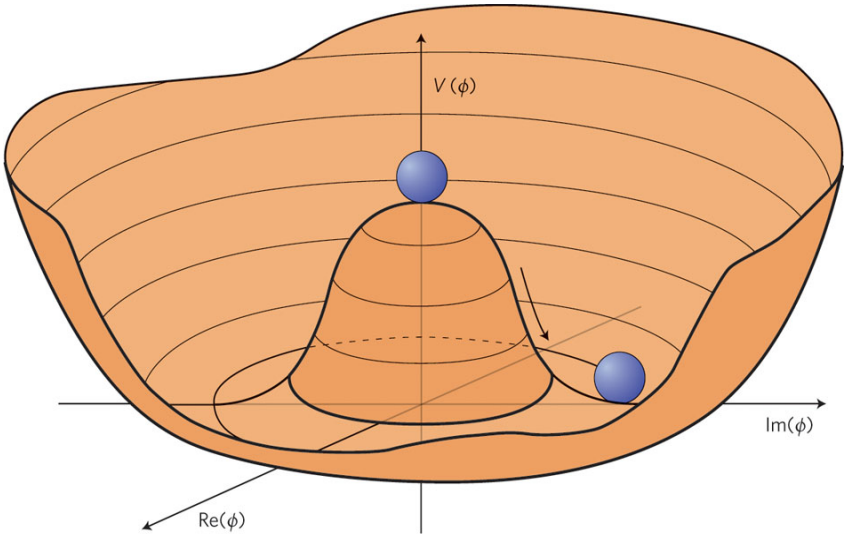

Figure 2.2: The "mexican hat" potential for the Higgs field. The potential is symmetric and as can be seen there are an infinite amount of ground states (minimas of the potential) to choose from that do not lie in the origo.

By choosing an appropriate formulation of the BEH mechanism, the Z and $W^{\pm}$ bosons will acquire mass and leave the photon massless. This is done by introducing one complex doublet

$$\phi = \frac{1}{\sqrt{2}} \begin{pmatrix} \phi_1 + i\phi_2 \\ \phi_3 + i\phi_4 \end{pmatrix}.$$

By introducing this type of field to the Lagrangian via the terms

$$\mathcal{L} = \frac{1}{2}(D_\mu \phi)(D^\mu \phi) + \frac{1}{2}\mu^2(\phi^* \phi) - \frac{1}{4}\lambda^2(\phi^* \phi)^2$$

we get a potential looking like a "mexican hat" shown in Fig. 2.2. The covariant derivative D_μ in the kinetic term ensures the gauge invariance of the field. The second two terms make up the potential. This potential is symmetric but the minimum is not located at $\phi = 0$, meaning it has a non-zero ground states. In order to use Feynman calculus one must pertubate around a ground state. In this case there are many to choose from (infinite amount of ground states exists) and when one is chosen the symmetry is no longer visible. Any minima will generate a mass for the corresponding gauge boson, but since we want one of the gauge bosons to remain massless we need to choose one ground state that is invariant under a subgroup of gauge transformations. If it is invariant under this subgroup the associated gauge boson will be massless. The minima that fulfills this is

$$\phi_1 = \phi_2 = \phi_4 = 0 \quad \text{and} \quad \phi_3 = v.$$

This choice of minima will as mentioned leave the photon massless. The weak vector bosons will gain mass and the three Goldstone bosons are absorbed by them as longitudinal polarizations. During this process another massive particle is generated, the Higgs boson, H with its corresponding Higgs field. It is its coupling to the fermions that generates the massive fermions' mass. The problem with the infinte diagram with several intermediate W bosons is also solved by the Higgs boson. Diagrams containing both the H boson and W bosons cancels the infinite contributions and a finite result is achieved.

Chapter 3

The LHC and the ATLAS Experiment

This chapter breifly describes the LHC (Large Hadron Collider) and the ATLAS detector that is used for looking for the Higgs boson among other things. A more detailed and technical description, which this chapter is based upon, can be found in [21, 22]. Before describing the LHC and ATLAS, a short introdution to the concept of luminosity is given since it is central in experimental particle physics.

3.1 Luminosity and Accelerators

Luminosity is the ratio of number of events N detected per time t and the cross-section σ:

$$\mathcal{L} = \frac{1}{\sigma}\frac{dN}{dt}.$$

Since the cross-section has the dimension of area, the luminosity has the dimension of events per time per area and is often measured in $\mathrm{cm}^{-2}\mathrm{s}^{-1}$. The luminosity of an accelerator depends on particle beam parameters, like beam width and particle flow rate, making it a useful indicator of the performance of the accelerator. Higher luminosity means more available data to analyze. A related quantity is the integrated luminosity defined as:

$$L = \int \mathcal{L} dt.$$

3.2 LHC

The LHC, built by the European Organization of Nuclear Research (CERN) between 1998 and 2008, is located beneath the border between Switzerland and France and is the world's largest and most powerful particle accelerator. Consisting of a 27 km ring of superconducting magnets, the LHC is placed underground, some parts up to 175 m below surface, in order to shield it from the cosmic rays.

There are several different experiments at the LHC looking for different phenomena such as the search for the Higgs boson (the main reason for the LHC), supersymmetry and dark matter. There are in total seven different detectors located on the LHC; ATLAS, CMS, ALICE, LHCb, TOTEM, MoEDAL and LHCf. Among these the ATLAS and CMS are multipurpose detectors and are used for looking for the Higgs particle and new high energy physics.

The LHC collides two opposing beams containing either protons or lead nucleus. The protons were collided with an energy of 3.5 TeV per beam during 2010 and 2011 and at 4 TeV in 2012. It was shut down in 2013 in order to upgrade it and will be running again in 2015 with a beam energy of 7 TeV for proton-proton collisions.

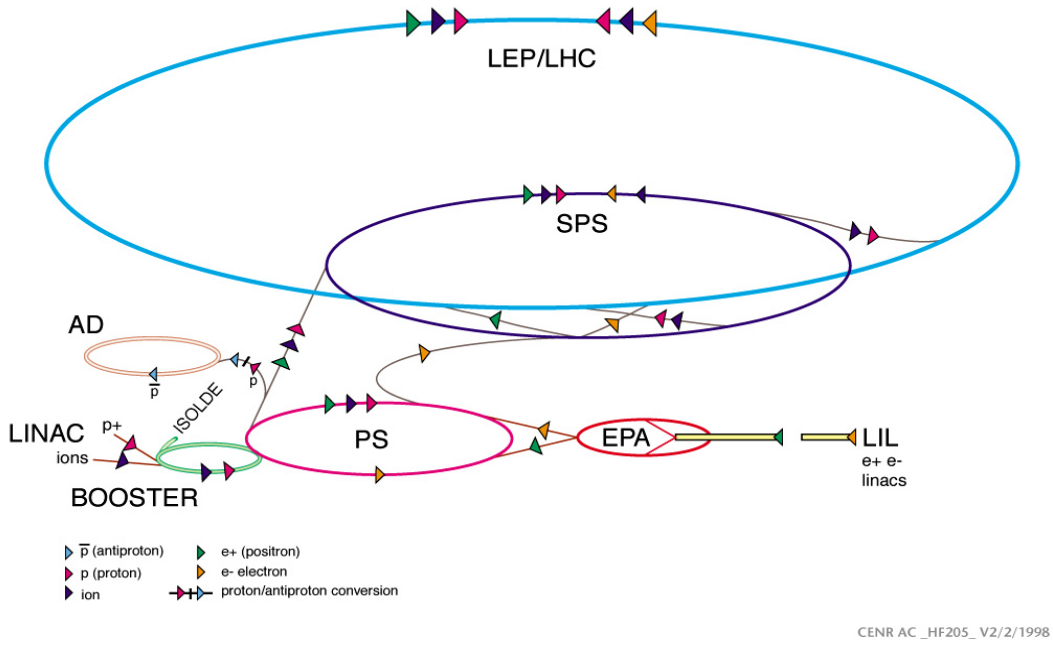

Figure 3.1: The accelerator complex at CERN. The protons are first injected in Linac2. From there they continue to Proton Synchrotron Booster and then to the Proton Synchrotron. After that they are injected to the Super Proton Synchrotron and at last into the LHC.

Before the protons enter the LHC they are accelerated in smaller accerlerators. The protons are procured by stripping hydrogen gas of electrons. They are then injected to Linac2, a linear accelerator that accelerates the protons to an energy of 50 MeV. They then continue on to the Proton Synchotron Booster (PSB) where the beam of protons are accelerated to 1.4 GeV. The next stop for the beam is the Proton Synchotron (PS) in which it gains a beam energy of 25 GeV. Before enerting the LHC the beams are injected to the Super Proton Synchotron (SPS) where they are acccelerated to an energy of 450 GeV. From the SPS the beam is them split in to two and then fed into the LHC ring. They are guided around the ring with the help of 1232 superconducting dipole magnets that generates an magnetic field of 8.4 T. This field bends the trajectory of the particles, making them go around the ring.

3.3 ATLAS Detector

The ATLAS detector, shown in Fig. 3.2, is 44 m long and 25 m tall and weighs approximately 7000 tonnes. It is designed to register collisions of protons with a collision energy up to 14 TeV at a luminosity of 10^{34} cm^{-2}s^{-1}. Beams accelerated in the LHC collide in the ATLAS detector and new particles are created and scattered away from the collision point. The new particles can then be identified by measuring their momenta and energy. Because the amount of collisions of particles are high, leading to high radiation, the detector is desgined to withstand this. The ATLAS detector is a multipurpose detector and therefore is required to be able to detect a wide variety of particles, jets and missing transverse energy. This means that it is important to be able to detect and specify what type of particles are detected in an event. Since there are many collsions when the detector is running there are many events that are recorded. But not all of these events contains new physics or the Higgs boson. It is therefore of importance to design a good trigger system that selects the events of interest.

The detector is divided into three main subsystems. The inner detector is closest to the beam pipe and tracks the path of the charged particle in the 2 T magnetic field. In the magnetic field, the path of the charged particles will bend. From the curvature of the path, the momenta of the particle can be calculated. Outside the inner detector is the elecromagnetic and hadronic calorimeters measuring the energy of the particles that are scattered. At the outermost part of the ATLAS detector is the muon system which measures the momentum of the muons coming from inside the detector.

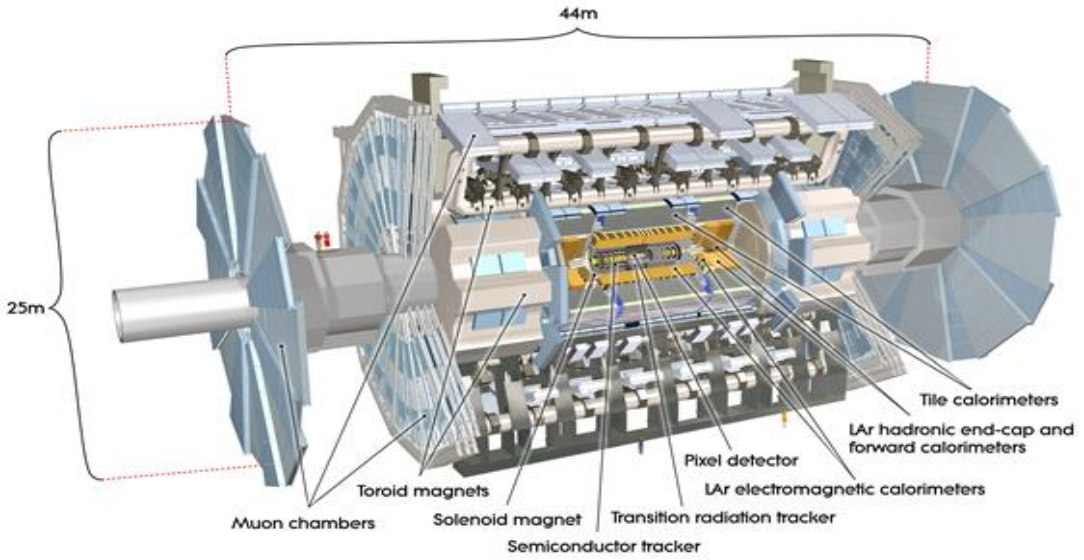

Figure 3.2: The ATLAS detector with all its subsystems.

Apart from these three subsystems the ATLAS detector also have forward detectors that are located in the LHC tunnel far away from the rest of the detector, so that scattering at very low angles can be detected.

Before presenting the different subsystems in more detail, the coordinate system used by the ATLAS exeriment is described.

3.3.1 Coordinate System

The nominal interaction point is defined at the orgin of the coordinate system. The beam direction then defines the z-axis, while the positve x-axis points from the interaction point towards the center of the LHC ring and the y-axis is pointing upwards. The pseudorapidity is defined as

$$\eta = -\ln \tan\left(\frac{\theta}{2}\right)$$

and describes the angle of the particle relative to the beam axis. Its value ranges from $\eta = 0$, that corresponds to $\theta = 90°$, to $\eta = \infty$, that corresponds to $\theta = 0°$.

3.3.2 Inner Detector

The inner detector, ID, contained in a solenoid that generates a magnetic field of 2 T, has a radius of 1.15 m and is 7 m in length. It covers $|\eta| < 2.5$ and consists of three complementary subdetectors: the Pixel Detector, the Semi-Conductor Tracker (SCT) and the Transition Radiation Tracker (TRT) [21]. The Pixel Detector and the SCT are both semiconductor tracking detectors while the TRT is a straw tube tracker.

At the inner radii, 5 cm up to 12 cm, the Pixel Detector is positioned. It consists of three concentric barrels and three disks at each end-cap. The layers are made up by silicon pixels with dimensions 50 μm $\times$ 400 μm. A total of 80 milion readout channels make up the Pixel Detector enabling it to make precise measurements of the particle's trajectories.

The SCT is also a silicon detector but instead of pixels it has eight layers of long and narrow strips of silicon with the dimensions 80 μm $\times$ 12 cm. It starts at a radius of 30 cm to 51 cm and has 6.3 milion readout channels. The SCT covers a larger area than the Pixel Detector and therefore improves the measurements by being able to sample more space points.

The outermost part of the ID is the TRT. It is made up by gaseous straw tubes that are aligned with the beam pipe in the barrel region. Each straw has a diameter of 4 mm and a length of 144 cm for the straws on the barrel and 37 cm for the ones at the end-cap. The gas in the straw tubes is ionized when charged particles pass through it. Since the straws are held at a voltage, the negative ions drift towards a wire at the center (the anode) and produces a current in the wire. Interspersed between the gaseous tubes are fibres (barrel) and foils (end-cap) that measures transition radiation which is needed for electron identification. The inner detector is shown in Fig. 3.4.

3.3.3 Calorimetry

The calorimeters measures the particles' energies. They are made up of sampling detectors that are symmetric in the ϕ-direction with $|\eta| < 4.9$. The calorimeters are

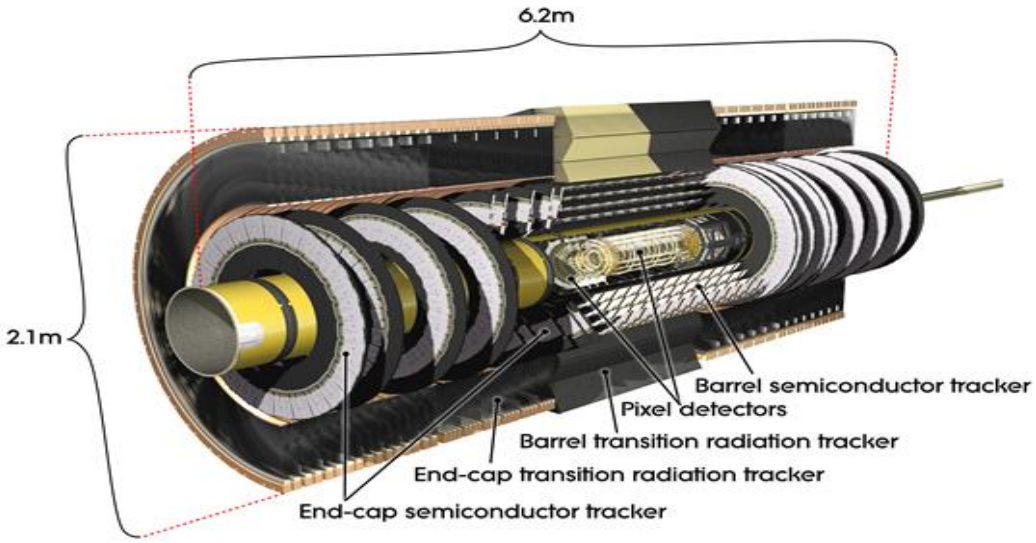

Figure 3.3: The ATLAS inner detector.

made up of alternating metal plates (absorbers) and detectors. The inner calorimeters are electromagnetic calorimeters (ECal) with lead-liquid argon detectors. The EM calorimeters consists of one electromagnetic barrel calorimeter, two elctromagnetic end-cap calorimeters (EMEC) and a forward calorimeter (FCal) [21]. These detectors have accordio-shaped absobers and electrodes allowing them to have many active layers in depth. The three of these can measure the particles in the range $0 < |\eta| < 2.5$ and two in the range $2.5 < |\eta| < 3.2$. The FCal provides measurements in the $3.1 < |\eta| < 4.9$ region.

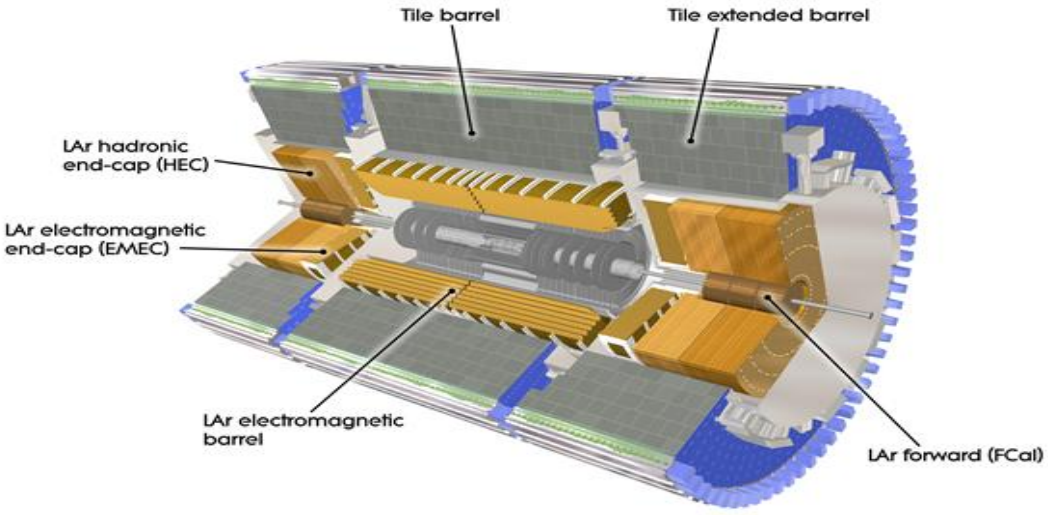

Figure 3.4: The ATLAS calorimeter system.

The hadronic calorimeters are positioned after the EM calorimeters. They consists of scintillator tiles as the sampling medium while the absorber is steel and are composed of

one central barrel, two extended barrel calorimeters and a end-cap hadronic calorimeter (HEC) that is located behind the EMEC. These calorimeters have a range of $0 < |\eta| < 1.7$ but with the help of the HEC and FCal can be extended to $|\eta| < 4.9$.

3.3.4 Muon Spectrometer

The muons are the only charged particles that can traverse the calorimeters without being absorbed. The muon spectrometer, shown in Fig. 3.5 is the outermost part of the ATLAS detector and it is large in order to get high precision measurements of the muon momentum in the pseudorapidity range $|\eta| < 2.7$ and also designed to trigger on the muons in the region $|\eta| < 2.4$.

The subsystem consists of a toroidal barrel and two end-cap magnets producing a magnetic field that bends the muon tracks enabling one to measure the momentum of the muons. The precsion measurement of the momentum is done by the The Monitored Drift Tube (MDT) chambers and the Cathode-Strip Chambers (CSC) [21]. The MDTs are tubes filled with gas. The electron that are released in the ionization (when the muons pass through tubes) are then collected by the anode wire in the middle of the tubes. The CSCs are a multiwire proportional chambers. They are have catode strips in the orthogonal directions of the chambers.

The triggering in the muon spectrometer is performed by the Resistive Plate Chambers (RPC) in the barrel region ($|\eta| < 1.05$) and by the Thin Gap Chambers (TGC) in the end-cap ($1.05 < |\eta| < 2.4$). The RPCs are gaseous parallell electrode-plate detectors. They are made up by two resistive plates with a potential over them. A signal is resigtered via capacitive coupling to metallic strips on the outer parts of the plates. The TGC not only triggers on the muons but also determines the azimuthal coordinate that complements the MDT's measurement of the bending of the muon tracks.

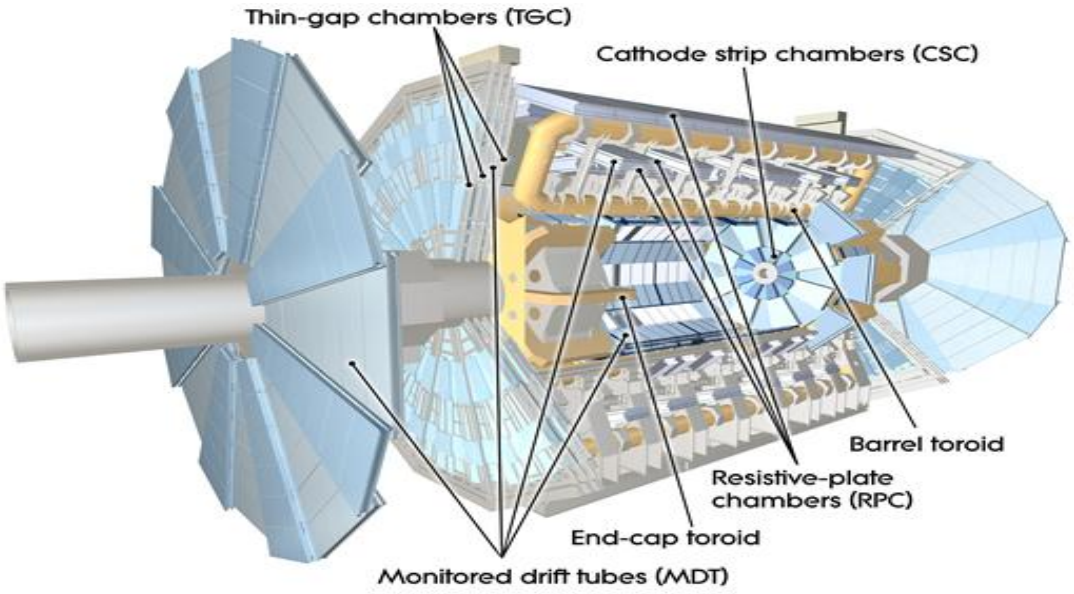

Figure 3.5: The muon spectrometer.

3.3.5 Forward Detectors

The forward detectors are used in order to detect the scatterings at small angles, to get the total luminosity. There are three smaller detectors ordered by distance. Closest to the interaction point is a Cerenkov detector named LUminosity measurement using Cerenkov Integrating Detector, LUCID. It is placed on both sides of the interaction point at a distance of 17 m and is the principal relative luminosity monitor in ATLAS. LUCID's main task is to detect forward p-p scattering and measure the integrated luminosity and online monitoring of the instantaneous luminosity and beam conditions. At a distance of 140 m, on both sides of the interaction point, the second forward dector is positioned. The Zero-Degree Calorimeter (ZDC) mainly detects forward neutrons with $|\eta| > 8.3$ in heavy-ion collisions. The third and furthermost forward detector is the Absolute Luminosity For ATLAS (ALFA) located at a distance of 240 m from the interaction point. Its main purpose is to measure the absolute luminosity, which can be done by measuring the forward scattering in an elastic scattering experiment (optical theorem).

3.3.6 The Trigger System

The trigger system selects relevant events that contains interesting information and possible new physics. The system consists of three subsystems; Level-1, Level-2 and the event filter. The Level-2 and the event filter make up the High-Level Trigger (HLT) that carries out calculations using data from the different subdetectors on the events selected by the Level-1 trigger. The Level-1 makes the initial event selection and it searches for traces from high transverse momentum muons, electrons, photons, jets and τ's decaying into hadrons. It also selects events with either large total transverse energy or large missing transverse energy. As the first trigger subsystem, Level-1 must make a decision if an event is to be selected fast, it has 2.5 μs to decide if an event is going to be sent forward to Level-2 or to be discarded.

If an event is selected by Level-1 it then reaches the Level-2 system. Here tracks can be calculated, from the coordinates from the detector, and energy determined. At this level a decision to keep a event and send it forward must be done in 40 ms. Because of this, Level-2 is able to do some more calculations that require more time than the ones made at Level-1.

The third and last part of the trigger system is the event filter that has up to 4 seconds to decide if the event is selected for permanent storage or if it is discarded.

3.4 Particle Detection

By combining data from the different subsytems the energy and the types of particles can be determined. Because of the magnetic fields applied charged particles will have a bending trajectory. As mentioned before, by measuring the amount of bending the momenta of the charged particle can be determined. Electrons and positrons leave tracks in the ID and deposits their energy in the EM calorimeter where the energy can be measured. The photons, having no eletric charge, do not bend in the magnetic field but is absorbed in the EM calorimeter as well and therefore the energy of photons are measured in the

EM calorimeter.

Since the quarks are never free but always bound to other quarks (hadrons), single quarks cannot be detected. The hadrons deposits their energy mainly in the hadronic calorimeter but also in the EM one. If the hadrons are charged, they will also leave a track in the ID. The jets are formed from the hadronization of quarks and are identified as cone shaped figures of particles that lie close to each other in the detecor. They leave energy in both the EM calorimeter and hadron calorimeter.

Muons can travel through almost the whole detector without being absorbed. They leave a track in the ID and deposit some of its energy in the calorimeters and some in the muon spectrometer. Muons with low energy can be identified by the by the tracking in the ID while muons with higher energy are easily indentifed by the muon spectrometer.

Neutrinos do not react that often with other particles and for this reason they go through the detector without leaving a trace. They are therefore identified by measuring the missing transverse energy, E_T^{miss}. The E_T^{miss} can be reconstructed by taking the negative vector sum of all the other particles' momenta.

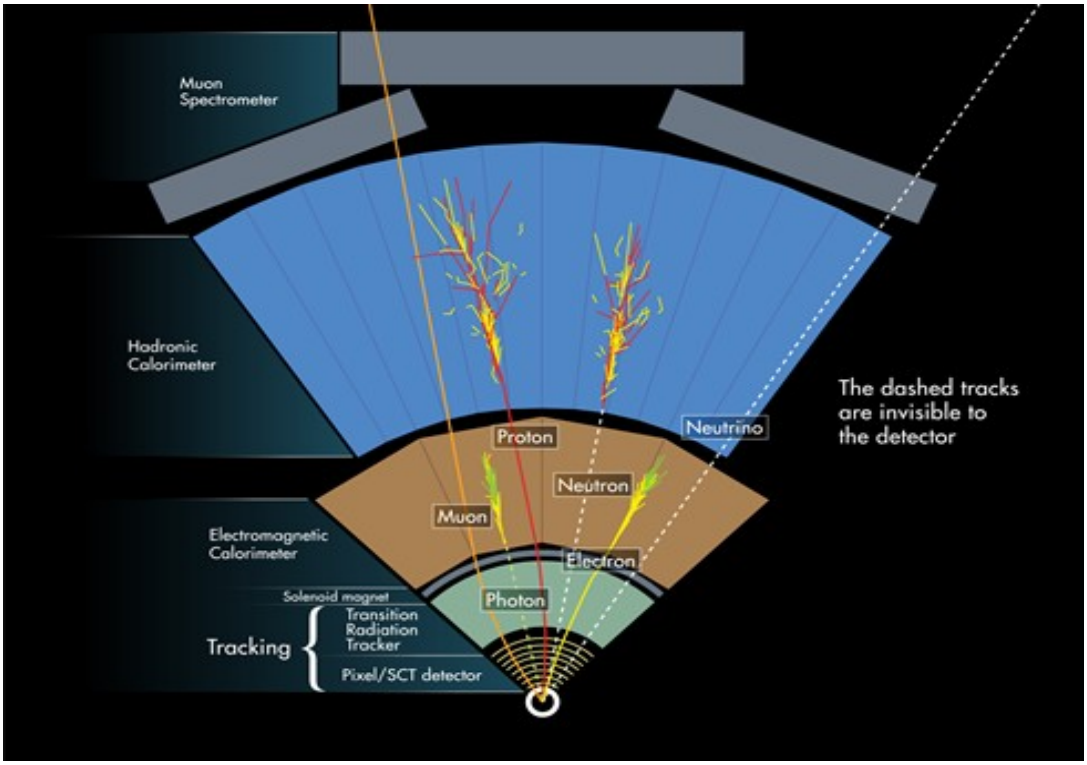

Figure 3.6: The tracks left by the different types particles in the ATLAS detector are used for particle identification.

Chapter 4

Higgs Boson Phenomenology

One of the main tasks for the LHC was to find the Higgs boson. The Higgs mechanism predicts the coupling between the boson and the other massive particles (except the neutrinos) leading to the many different decay paths for the Higgs boson. It does not, however, predict the mass of the Higgs boson itself. This complicates the process of designing experiments that are suitable to detect the particle. The coupling between the Higgs boson and massive particles is proportional to the mass of that particular particle (mass squared for the massive gauge bosons) meaning that heavier particles couples more strongly to the Higgs boson. In this chapter, based on Griffiths' book [13], some of the different production and decay processes that are used at the LHC are presented.

4.1 Higgs Boson Production

In order to produce Higgs bosons, heavier particles like the t quark or the weak gauge bosons, are needed. Since the LHC is mainly a p-p collider the dominant process for creating a Higgs particle at the LHC is the gluon 'fusion' mechanism, $gg \to H$, proceeding via a quark loop. The loop is mainly a t quark loop since it's the heaviest and couples most strongly to the boson.

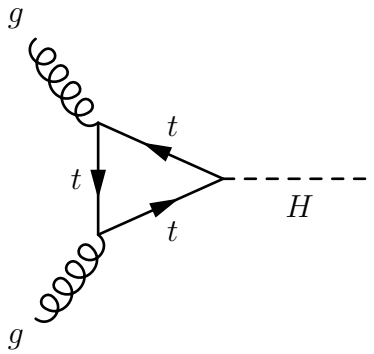

Figure 4.1: Feynman diagram of gluon fusion. All the quarks contribute in the loop. Since the t quark is the most massive its contributions dominates.

Other processes that can contribute to the Higgs productions are the vector boson fusion and W/Z-bremsstrahlung. For the vector boson fusion two quarks radiates a vector boson each. The bosons then annihilates to produce a Higgs boson. In the W/Z-bremsstralung process a quark and an anti-quark annihilates and produces a virtual vector boson ($W^{\pm}$

or Z) that decays into a real vector boson and a Higgs boson. Lastly, another production channel that is considered is the $q\bar{q}$-fusion where a pair of gluons or an quark/antiquark pair each. An quark from one of the pairs annihilates with the antiquark from the other pair to create a Higgs boson. The dominant quark in this reaction is the top quark since it is the most massive one.

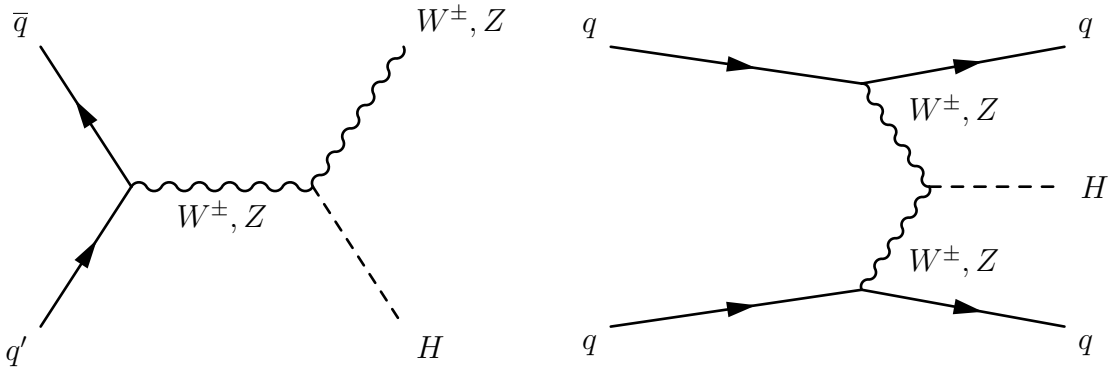

Figure 4.2: The W/Z-bremsstrahlung and vector boson fusion are also common production channels.

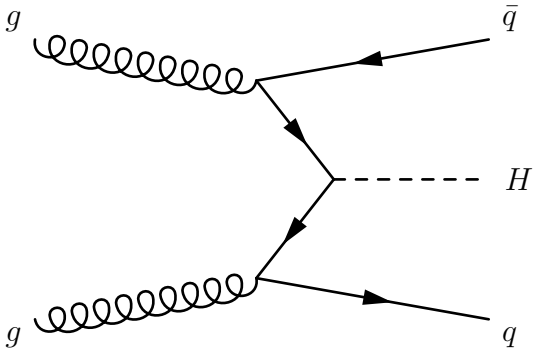

Figure 4.3: Feynman diagram of $q\bar{q}$ fusion. Any quark can contribute to this channel but since the t quarks couples most strongly it dominates.

The cross section for the different processes depend on the mass of the Higgs boson and before the Higgs mass was known it was kept as a variable in the cross section expression. The cross sections for the different production channels as a function of the Higgs mass are shown in Fig. 4.4 [23]. Now that the Higgs mass is known, the cross sections for the production channels are determined and are given in Tab. 4.1.

4.2 Higgs Boson Decays

Considering that the Higgs boson couples more strongly to heavier particles like $W^{\pm}, Z$ bosons and t quarks, it is more likely that it decays to these particles if they are kinematically available. The different branching ratios, the fraction of decays that lead to a particular final state, depend on the mass of the Higgs boson, as can be seen in Fig. 4.5.

If the Higgs boson mass is less than 140 GeV, which is now confirmed, the main decay process is the $H \rightarrow b\bar{b}$ seen in Fig. 4.6. The b-quarks would then be fragmenting to jets. This decay mode is unfortunately hard to distinguish from other processes with jets

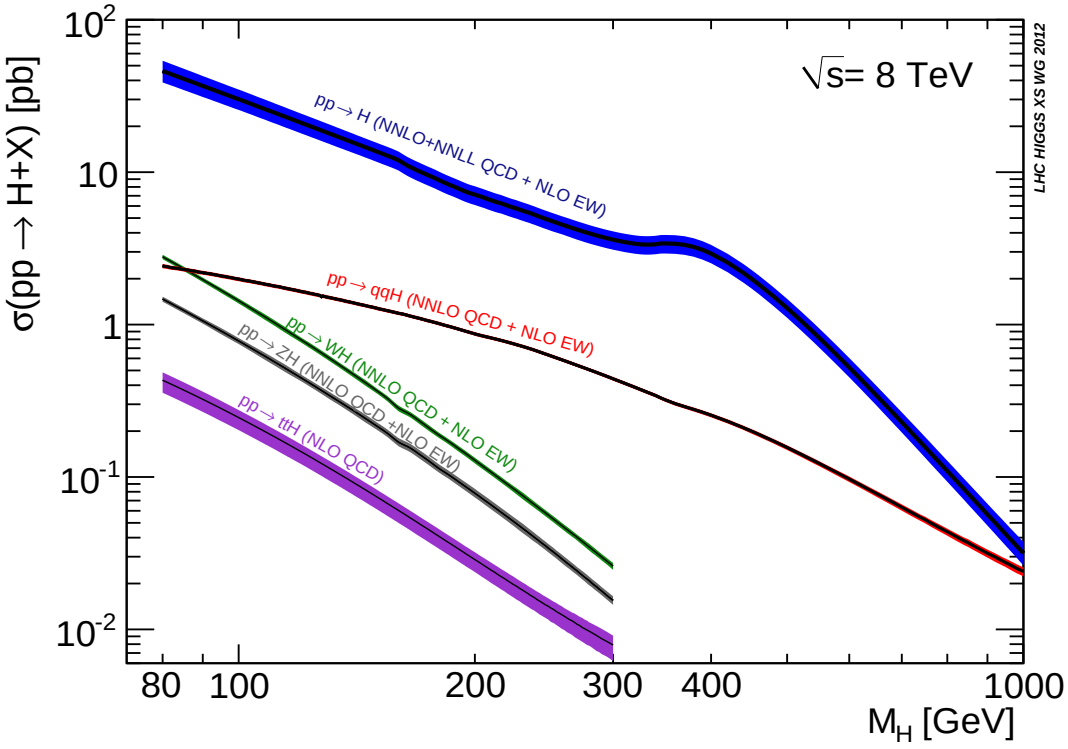

Figure 4.4: The cross sections for the main Higgs production channels as a function of m_H. The values correspond to the discovered boson at $m_H = 125$ GeV.

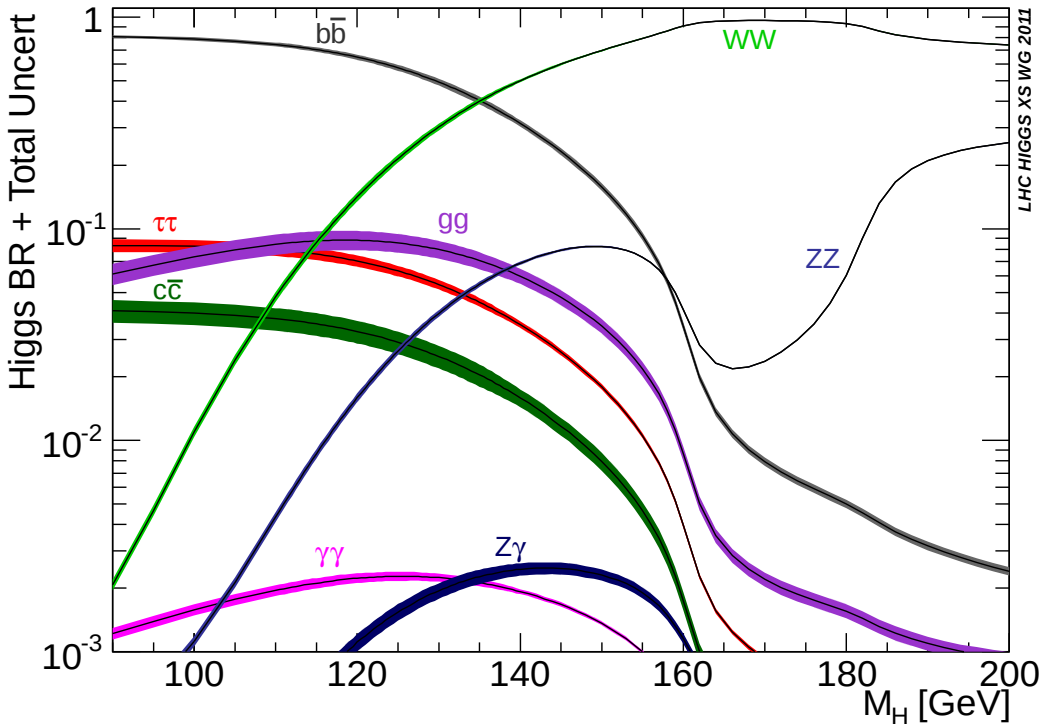

Figure 4.5: The branching ratios for different Higgs decay channels as a function of m_H. The values correspond to the discovered boson at $m_H = 125$ GeV.

Process	Name	Detonation	σ (pb)
$gg \to H$	Gluon-gluon fusion	ggF	19.27
$qq \to V^*V^* \to qq + H$	Vector boson fusion	VBF	1.58
$q'\bar{q} \to V + H$	W/Z-bremsstralung	WH/ZH	0.70 (WH) and 0.42 (ZH)
$gg \to q\bar{q} + H$	$q\bar{q}$-fusion	$t\bar{t}H$	0.13

Table 4.1: Table of Higgs production channels with their corresponding cross sections for $m_H = 125$ GeV at center of mass energy of 8 TeV.

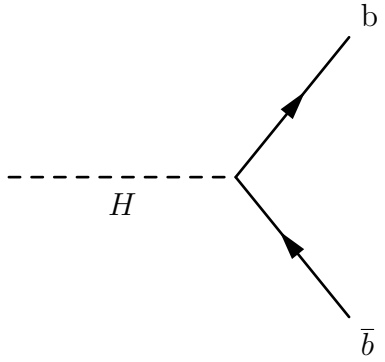

Figure 4.6: Feynman diagram of the $H \to b\bar{b}$ process, the main decay process for the Higgs boson with $m_H = 125$ GeV.

produced, making other modes more useful even if the the branching ratios are not as big. An interesting process is the decay into two high energy photons, $H \to \gamma\gamma$. The branching ratio for this decay is very small (order of 10^{-3}) [24]. This channel is very clean since the signal is clear. The two photons can be completely reconstructed giving a good measurement of the mass of the Higgs boson.

Two other decay modes that are most sensitive for finding Higgs bosons at the LHC are the decay to two W bosons and to two Z bosons. Both can then decay to four leptons, $H \to WW \to l\nu l\nu$ and $H \to ZZ \to l^+l^-l^+l^-$ These do also have smaller branching ratios than the $H \to bb$ but not as much background which is preferable.

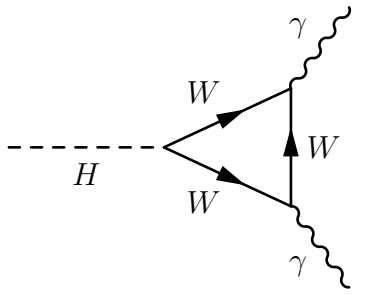

Figure 4.7: The $H \to \gamma\gamma$ process. A channel with a clean signal but small branching ratio.

The actual amount of Higgs boson events is given by the product of the cross section for the Higgs production and the branching ratio for a certain decay mode, see Fig. 4.8.This quantity is measured at CERN by both the ATLAS and the CMS experiments. As mentioned previously, the Higgs boson has many decay modes. Modes with high branching ratios are not necessarily the best modes to study because of the background processes. It is vital to be able to tell the Higgs events apart from the background in order to get a reliable result.

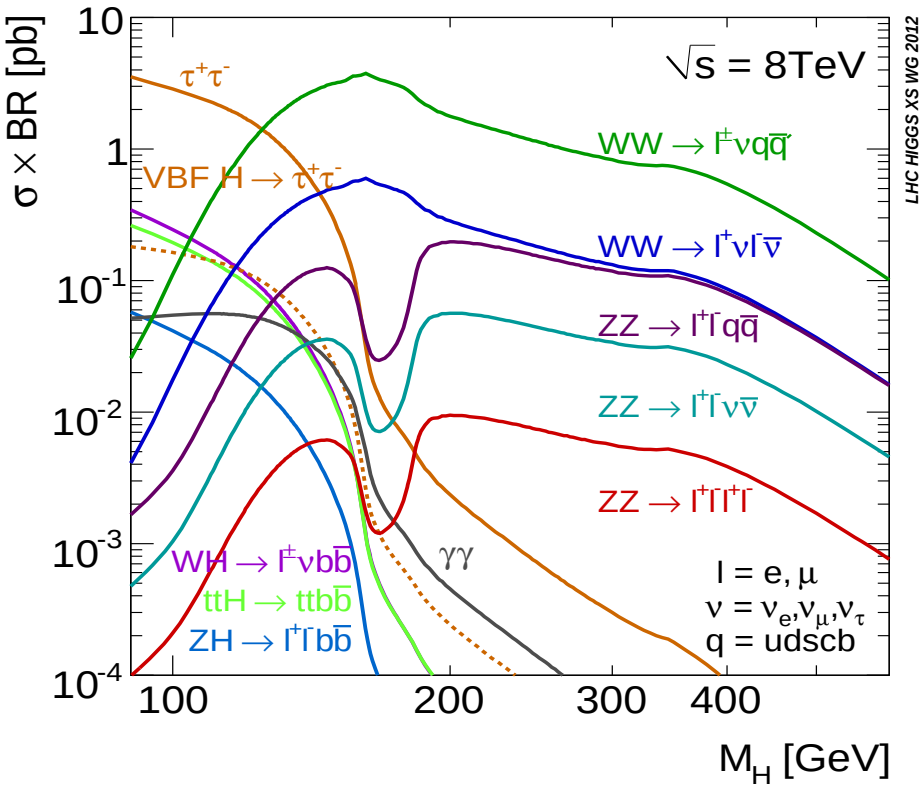

Figure 4.8: The total cross section of the Higgs boson decay modes as a function of m_H.

Chapter 5

Analysis of the $H \to WW^* \to l\nu l\nu$ Channel

In 2012, the CMS and ATLAS experiments discovered a Higgs-like boson with a mass of approximately $m_H = 125$ GeV [25, 26]. Many different decay channels are and have been studied for the Higgs boson in order to determine its properties. In this chapter the updated analysis of the dilepton channel, $H \to WW^* \to \ell\nu\ell\nu$, is descibed [27]. The re-optimized analysis improves the background estimation and expands phase space region in order to increase signal acceptance.

Since the Higgs mass is $m_H = 125$ GeV it cannot decay into two real W boson, meaning that one the the W bosons is virtual, denoted W^*. The ggF and VBF are the main production channels and are the ones that are considered in this analysis. Feynman diagrams for these two production and decay processes are shown in Fig. 5.1.

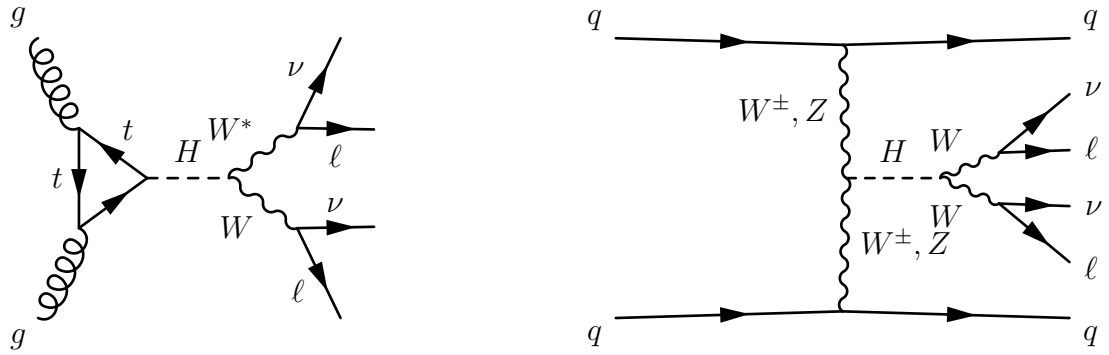

Figure 5.1: Feynman diagram for the $H \to WW^* \to \ell\nu\ell\nu$ decay channel with the ggF and VBF production modes respectively.

The $H \to WW^*$ decay mode has a branching ratio of 22% making it the decay mode with the next largest branching ratio after $H \to b\bar{b}$ [23]. The decay $WW^* \to \ell\nu\ell\nu$ occurs 10.5% of the times. This makes this channel good for measuring properties of the Higgs boson. Although this channel cannot determine the mass of the Higgs boson, because of the two neutrinos in the final state, it is an important channel for probing the couplings between the Higgs boson and the weak bosons. For this reason an alternative variable is defined - the transverse mass given by

$$m_T = \sqrt{(E_T^{\ell\ell} + E_T^{miss})^2 - |\mathbf{p}_T^{\ell\ell} + \mathbf{E}_T^{miss}|^2}$$

where $E_T^{\ell\ell} = \sqrt{|\mathbf{p}_T^{\ell\ell}|^2 + m_{\ell\ell}^2}$. The transverse mass is used to measure the signal strength.

The rate analysis, the measurering of the cross section of Higgs bosons events, is done in two steps; event selection and the statistical treatment. The details concerning these two steps are given below.

5.1 Data and Simulated Samples

Data was taken from the ATLAS detector in 2011 and 2012 with a centre of mass energy $\sqrt{s} = 7$ and 8 TeV respectively. The data is compared with simulated samples in order to estimate the fraction of the event that comes from our signal, the Higgs events. Monte Carlo, MC, generators are used to model both the signal and background processes and different generators are used for different parts (hard scattering, parton showers and hadronization) of the processes. The generators used are listed in [27].

For the simulated events only the ggF, VBF and WH/ZH production channels are considered. The ggF cross section is computed up to next-to-next-to-leading order (NNLO) in QCD with next-to-leading order (NLO) electroweak (EW) corrections and QCD soft-gluon resummations up to next-to-next-to-leading-log (NNLL) [27]. The VBF cross section is computed with approximate NNLO QCD corrections and full NLO QCD and EW corrections while WH/ZH is computed up to NNLO QCD corrections and NLO EW corrections.

In order to eliminate bias in the analysis regions where the signal dominate are removed. This process is called blinding. By blinding the data the estimation of the background and control regions can be better investigated. Once the blinded data is analysed the data is unblinded.

5.2 Selection of Events

The first part of the analysis is the event selection. A series of cuts (conditions) on the events, are applied in order to collect the events of interest. Different cuts are applied depending on if the leptons have the same flavor (ee or $\mu\mu$) or different ($e\mu$ or μe) flavor and the number of jets in the event.

5.2.1 Pre-selection

The basic cuts that are applied are called the pre-selection cuts. They are given below:

- Exactly two isolated leptons with $p_T > 22$ GeV for the leading lepton and $p_T > 10$ GeV for the sub-leading lepton.
- $m_{\ell\ell} > 10$ GeV for $e\mu/\mu e$ and > 12 GeV for $ee/\mu\mu$.

- $|m_{\ell\ell} - m_Z| > 15$ GeV (Z-Veto)

The events should have exactly two isolated leptons (e or μ) of opposite charge, since the Higgs boson is neutral. It is also required that the leading lepton has a transverse momenta $p_T > 22$ GeV and the sub-leading $p_T > 10$ GeV since we expect leptons with high momenta in this channel. The next cuts are put in to filter out the Drell-Yan processes that also gives rise to two leptons with opposite charge. Drell-Yan, DY, processes are present in hadron-hadron scattering with high energy. A quark from one hadron annihilates with an antiquark from another hadron can creates an virtual photon or Z boson that then decays to two oppositely charged leptons. In order to filter out the background process $Z \to \ell\ell$ the Z-Veto cut is implemented around resonance region.

The last pre-selection cut is on the missing transverse energy, MET. Since the final states contains neutrinos, conditions on the missing transverse energy is required. A more discriminating variable for the missing transverse energy is defined as

$$E_{T,rel}^{miss} = \begin{cases} E_T^{miss} & \text{if } \Delta\Phi \geq \pi/2 \\ E_T^{miss} \sin\Delta\Phi & \text{if } \Delta\Phi < \pi/2. \end{cases}$$

$\Delta\Phi$ is the angle between the $\mathbf{E}_T^{miss}$ and the nearest lepton or jet. There are also many other types of missing transverse energy variables used in the $H \to WW^* \to \ell\nu\ell\nu$ analysis. For the same flavor channel, the Z/DY background is the most dominant. These events do not involve neutrinos meaning that if E_T^{miss} is non-zero, it is coming from not being able to measure the quantity accurately. For this reason E_T^{miss} is a important discriminating variable.

The events passing the missing transverse energy cut are then subjected to different cuts depending on their jet multiplicity. Different backgrounds are of more inportance depending on the number of jets in an event. The section below will descibe the analysis for ggF $N_{jet} = 0, 1$ analysis focusing on $N_{jet} = 1$. There are also analysis for $N_{jet} > 2$ and VBF production channel but these are omitted in this thesis and can be found in [27].

5.2.2 ggF $N_{jet} = 0$ Analysis

Since the Higgs boson is a spin-0 particle, the two W bosons must have opposite spin to conserve angular momentum. The W bosons then decay in to an e^-/μ^- and $\bar{\nu}$ or to an e^+/μ^+ and ν depending on the charge of the boson. Conservation of angular momentum requires that that the charged leptons are in the same direction and the neutrinos in the opposite direction. This means that the invariant dilepton mass, $m_{\ell\ell}$, defined as

$$m_{\ell\ell} = \sqrt{(E_{\ell^+} + E_{\ell^-})^2 - |\mathbf{p}_{\ell^+} + \mathbf{p}_{\ell^-}|^2},$$

will be small for parallell charged leptons. It also means that the angle bewteen the charged leptons, $\Delta\phi_{\ell\ell}$, is small and that the angle between E_T^{miss} and the charged leptons, $\Delta\phi_{\ell\ell,E_T^{miss}}$, is large. Lastly, because of the recoil from the leptons the DY background can be further suppressed using the f_{recoil} variable. f_{recoil} measures the hadronic recoil

that is produced opposite to the two charged leptons. In DY processes, no neutrinos are created and f_{recoil} will be large. By requiring a small value on this variable, those events can be supressed.

The selection cuts for events with the ggF production channel and $N_{jet} = 0$ that are applied in the analysis are

- $E_T^{miss,J-TRK} > 20$ GeV for $e\mu/\mu e$ and $E_{T,rel}^{miss,CAL} > 40$ GeV for $ee/\mu\mu$
- $m_{\ell\ell} < 55$ GeV
- $\Delta\phi_{\ell\ell} < 1.8$ radians
- $p_T^{\ell\ell} \geq 30$ GeV
- $\Delta\phi_{\ell\ell,E_T^{miss}} > \pi/2$
- $f_{recoil} < 0.1$ and $E_{T,rel}^{miss,TRK} > 40$ GeV for $ee/\mu\mu$.

5.2.3 ggF $N_{jet} = 1$ Analysis

The events in this channel must have exactly one jet with $p_T > 20$ GeV and no b-tag. Channels with jets have a significant top background, $t\bar{t}$ and Wt events leading to WW events. Most of these events lead to b-tagged jets (since most top quarks decay to bottom quarks) and thus by requiring that no b-tagged jets are present, these events can be supressed.

A cut on the invariant mass for $Z \to \tau\tau$ mode is applied to reduce that background. The transverse mass, M_T^W, is requied be large for both of the charged leptons. Leptonic decays with one or more real W bosons have at least one lepton with high M_T^W. By having a lower bound on this variable the $Z \to \tau\tau$ events can be rejected.

The cuts for the $N_{jet} = 1$ channel that are applied after the pre-selection cuts are therefore given by

- $E_T^{miss,J-TRK} > 20$ GeV for $e\mu/\mu e$ and $E_{T,rel}^{miss,CAL} > 40$ GeV for $ee/\mu\mu$
- b-jet veto
- $m_{\tau\tau} < |m_Z - 25|$ GeV
- $M_T^W > 50$ GeV
- The event must satisfy the cuts on $m_{\ell\ell}$ and $\Delta\phi_{\ell\ell}$ described in the analysis for ggF $N_{jet} = 0$
- $E_{T,rel}^{miss,TRK} > 35$ GeV and $f_{recoil}^{extended} < 0.1$ for $ee/\mu\mu$.

5.3 Backgrounds and Control Regions

In order to determine if there are excess events coming from the decay of the Higgs boson one must estimate the amount of background events present. This is done by calculating the number of background events in a control region (CR), a region of phase space where the particular background is maximized. This is then extrapolated to the signal region (SR), a region of phase space where the signal dominates, by multiplying the number of events in CR with the extrapolation factor defined as

$$\alpha = \frac{N_{SR}^{MC}}{N_{CR}^{MC}}.$$

The extrapolation factor is the ratio bewtween the number of background events in SR and the number of background events in CR given by the MC simulations.

The background composition depends on the jet multiplicity, different background events dominate depending on the number of jets present. This can be seen in Tab. 5.2 for Higgs events produced via ggF. In this section, the main backgrounds and their respective CR are presented for the $N_{jet} = 1$ channel.

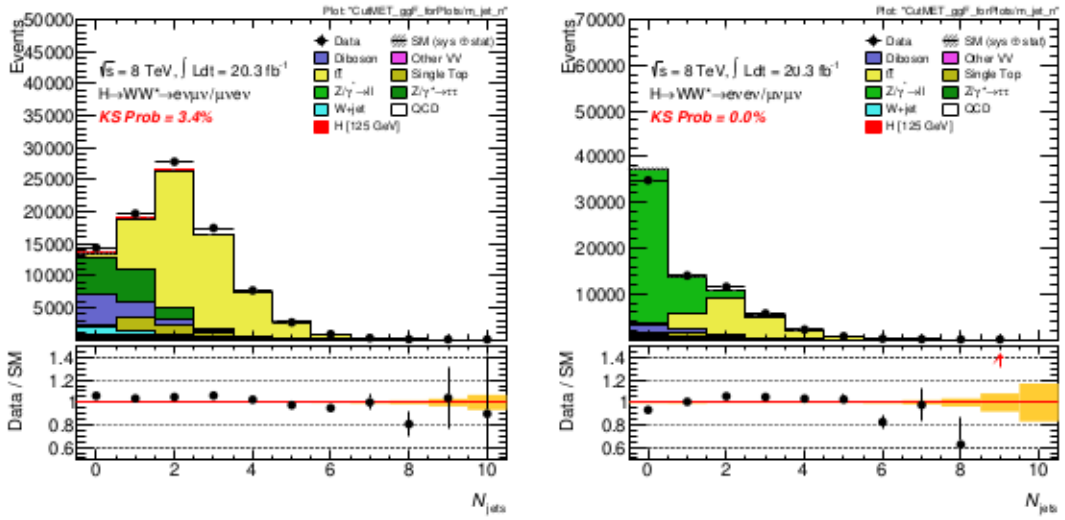

Figure 5.2: The distribution of jet multiplicity after the pre-selection cuts for ggF production. The left plot shows the distribution for different flavor and the right shows the distribution for same flavor.

5.3.1 $W+$ jets Background and Control Region

The $W+$ jets background arise when a jet is misidentified as a lepton. This background is estimated from data since it is difficult to simlulate. The CR for this background is formed by one lepton passing the requirements for the SR. The other object does not pass these requirements, but it does pass a looser criteria. Such a lepton is denoted as anti-identified. The estimation of this background in the SR is done by a extrapolation factor called *fake factor*. It is defined as

$$f = \frac{N_{id}}{N_{anti-id}}$$

where N_{id} is the number of leptons satisfying the SR criteria and $N_{anti-id}$ is the number of objects mis-indentified as leptons [28]. The fake factor is measured in the data from the $N_{jet} = 2$ and $Z+$ jet events. The $W+$ jets background in the SR is then calculated by multiplying the number of events in the $W+$ jets CR, $N^{CR}_{W+\text{jets}}$, with the fake factor

$$N_{W+\text{jets}} = f \cdot N^{CR}_{W+\text{jets}}.$$

5.3.2 DY Background and Control Region

The treatment of the DY background differs in the same flavor and different flavor channels. In the different flavor channel the DY background comes from $Z/\gamma^* \to \tau\tau$ where the tauons decay leptonically. These events generates high missing transverse energy. The CR for $N_{jet} = 1$ is defined by the pre-selection cuts, b-veto, $M_T^W > 50$ GeV and the following

- $m_{\ell\ell} < 80$ GeV
- $m_{\tau\tau} > 66$ GeV [29].

In the same flavor channel the DY background enters as $Z/\gamma^* \to ee/\mu\mu$. In this case, there is no real missing transverse energy present but mis-measuring leads to non-zero E_T^{miss}. Because there are no real neutrinos in this event the two leptons must be balanced by a hadronic recoil system. The amount of hadronic activity opposite the dilepton system is measured by the f_{recoil} variable. It has different shapes for a DY process and a non-DY process making it possible to discriminate these two.

5.3.3 WW Background and Control Region

The $WW^{(*)} \to \ell\nu\ell\nu$ is the main background in the $N_{jet} = 0$ channel (65% of the total background) and in the $N_{jet} = 1$ channel (40% of the total bakground) [28]. This background contains two isolated high-p_T charged leptons and large E_T^{miss} from W decays, similar to the signal. It is normalized from data using a region that differs from the signal region (SR) in the range of dilepton invariant mass. For $N_{jet} = 1$ range is $m_{\ell\ell} > 80$ GeV. Because of the abundance of DY events in this control region for the same flavor channel, only the events from different flavor are used in the normalization. Similarily, the WW CR is not used in $N_{jet} \geq 2$ for the amount of top background present and therefore estimatated entirely from MC simulations.

5.3.4 Top background and Control Region

The top quark's most dominant decay mode is $t \to Wb$, and makes up a significant part of the background for $N_{jet} = 0, 1$. The top events of interest are $t\bar{t}$ and single top (Wt, tb and tqb) and are mostly supressed by tagging the b quarks. The top CR for $N_{jet} = 1$ is defined by the pre-selection cuts and some of the signal cuts:

- $E_T^{miss,J-TRK} > 20$ GeV
- $\Delta\phi_{\ell\ell} < 2.8$ for $e\mu/\mu e$
- $E_{T,rel}^{miss,CAL} > 40$ GeV for $ee/\mu\mu$

At least one b-tagged jet is also required with a $p_T > 20$ GeV. The top background will be discussed more in the next chapter.

5.4 Statistical Treatmeant

The statistical analysis of the data is evaluated through a likelihood ratio test. It is used to compare two hypothesis and evaluate which one fits the data best. The two hypothesis tested are: "the observed data comes only from SM background process" and "there is an excess signal from a 125 GeV Higgs boson". The likelihood ratio test is based on a ratio that expresses how many more times the data supports one hypothesis over the other.

The testing variable in the $H \to WW^* \to \ell\nu\ell\nu$ is the transverse mass, m_T [27]. A likelihood function, $\mathcal{L}$, is used for the statistical analysis. It is given by a product of Poisson functions (over the decay channels) for all the SR and CR regions and gaussian constraints. The SR part of $\mathcal{L}$ is given by

$$\mathcal{L}(\mu, \mu_b) = P\Big(N|\mu s + \mu_b \sum_i^{N_{bkg}} b_{SR}^{exp}\Big)$$

where s and b_{SR}^{exp} are the expected yield for signal and background in the signal region given by MC calculations. μ is the signal strength parameter and μ_b the background strength parameter. The value of the signal parameter determines which hypothesis is supported by data. $\mu = 0$ correspond to no signal while $\mu = 1$ corresponds to a SM Higgs boson. It is defined as

$$\mu = \frac{\sigma_H^{data}}{\sigma_H^{SM}},$$

where σ_{SM} is the calcualted cross section for the Higgs boson with m_H =125 GeV.

In addition to the strength parameter, so-called nuisance parameters, $\boldsymbol{\theta}$ are added to the likelihood function in order to take into account the systematic uncertainties in the analysis. The nuisance paramters affects the expected yields for the signal and background and they are Gaussian or Poisson shaped in the likelihood function.

When the likelihood function is obtained, the likelihood ratio

$$\lambda(\mu) = \frac{\mathcal{L}(\mu, \hat{\hat{\boldsymbol{\theta}}}(\mu))}{\mathcal{L}(\hat{\mu}, \hat{\boldsymbol{\theta}})}$$

is calculated. $\hat{\hat{\boldsymbol{\theta}}}$ is the value of the nuisance vector that maximizes $\mathcal{L}$ for the assumed μ. In the denominator, the values $\hat{\mu}$ and $\hat{\boldsymbol{\theta}}$ maximizes the likelihood without constraint. For this reason, $0 < \lambda(\mu) < 1$ and the maximum value is reached when μ is equal to $\hat{\mu}$, meaning that the data supports the hypothesis [30]. If $\hat{\mu} < 0$, it is set to zero since negative signal rate is not expected.

From the likelihood ratio the test statistic is obtained by taking

$$q_\mu = -2 \ln \lambda(\mu).$$

From this the modified frequentist method CL is used to compute 95% confidence intervals on the signal strength parameter [27].

5.5 Results

The updated analysis for the data collected at the LHC during the years 2011 and 2012 is still ongoing during the writing of this thesis. The results have yet to be published, but the previous analysis of the same data is given below.

The expected and observed yields for the signal and background processes for the 8 TeV data for the different jet multiplicities are given in Tab. 5.1 [31]. The yields include both different and same flavor and both the systematic and statistical uncertainties are included.

N_{jet}	N_{obs}	N_{bkg}	N_{sig}	N_{WW}	N_{VV}	$N_{t\bar{t}}$	N_t	N_{Z/γ^*}
= 0	831	739 ± 39	97 ± 20	551 ± 41	58 ± 8	23 ± 3	16 ± 2	30 ± 10
= 1	309	261 ± 28	40 ± 13	108 ± 40	27 ± 6	68 ± 18	27 ± 10	12 ± 6
≥ 2	55	36 ± 4	10.6 ± 1.4	4.1 ± 1.5	1.9 ± 0.4	4.6 ± 1.7	0.8 ± 0.4	22 ± 3

Table 5.1: The expected and observed yield for the 8 TeV data for the signal and background processes.

Tab. 5.2 shows a cutflow table for the $N_{jet} = 1$ different flavor channel for the 8 TeV data. The expected and observed yields at the different selection cuts are given for the signal and background processes. The distributions of the m_T, the variable used to measure the strength parameter, for the $N_{jet} = 0$ and $N_{jet} = 1$ channel are given in Fig. 5.3.

Since the $H \to WW^* \to \ell\nu\ell\nu$ has neutrinos in the final state, total mass reconstruction is not possible. Other channels have measured the mass of the Higgs boson accurately to $m_H = 125$ GeV and this value has been used as a benchmark for the analysis for this channel. The signal strength for the 2013 analysis at this mass, with a signal significance of 3.8 standard deviations, is

$\mu_{obs} = 1.01 \pm 0.21$ (stat.) ± 0.19 (theo. syst.) ± 0.12 (expt. syst.) ± 0.04 (lumi.) $= 1.01 \pm 0.31$.

Selection	N_{obs}	N_{bkg}	N_{sig}	N_{WW}	N_{VV}	$N_{t\bar{t}}$	N_t	N_{Z/γ^*}
$N_{\text{jet}} = 1$	9527	9460 ± 40	97 ± 1	1660 ± 10	270 ± 10	4980 ± 30	1600 ± 20	760 ± 20
$N_{b\text{-jet}} = 0$	4320	4240 ± 30	85 ± 1	1460 ± 10	220 ± 10	1270 ± 10	460 ± 10	670 ± 10
$Z \to \tau\tau$ veto	4138	4020 ± 30	84 ± 1	1420 ± 10	220 ± 10	1220 ± 10	440 ± 10	580 ± 10
$m_{\ell\ell} < 50$	886	830 ± 10	63 ± 1	270 ± 4	69 ± 5	216 ± 6	80 ± 4	149 ± 5
$\lvert\Delta\phi_{\ell\ell}\rvert < 1.8$	728	650 ± 10	59 ± 1	250 ± 4	60 ± 4	204 ± 6	76 ± 4	28 ± 3

Table 5.2: Cutflow for the $N_{jet} = 1$ different flavor channel for $\sqrt{s} = 8$ TeV. The uncertainties included are statistical.

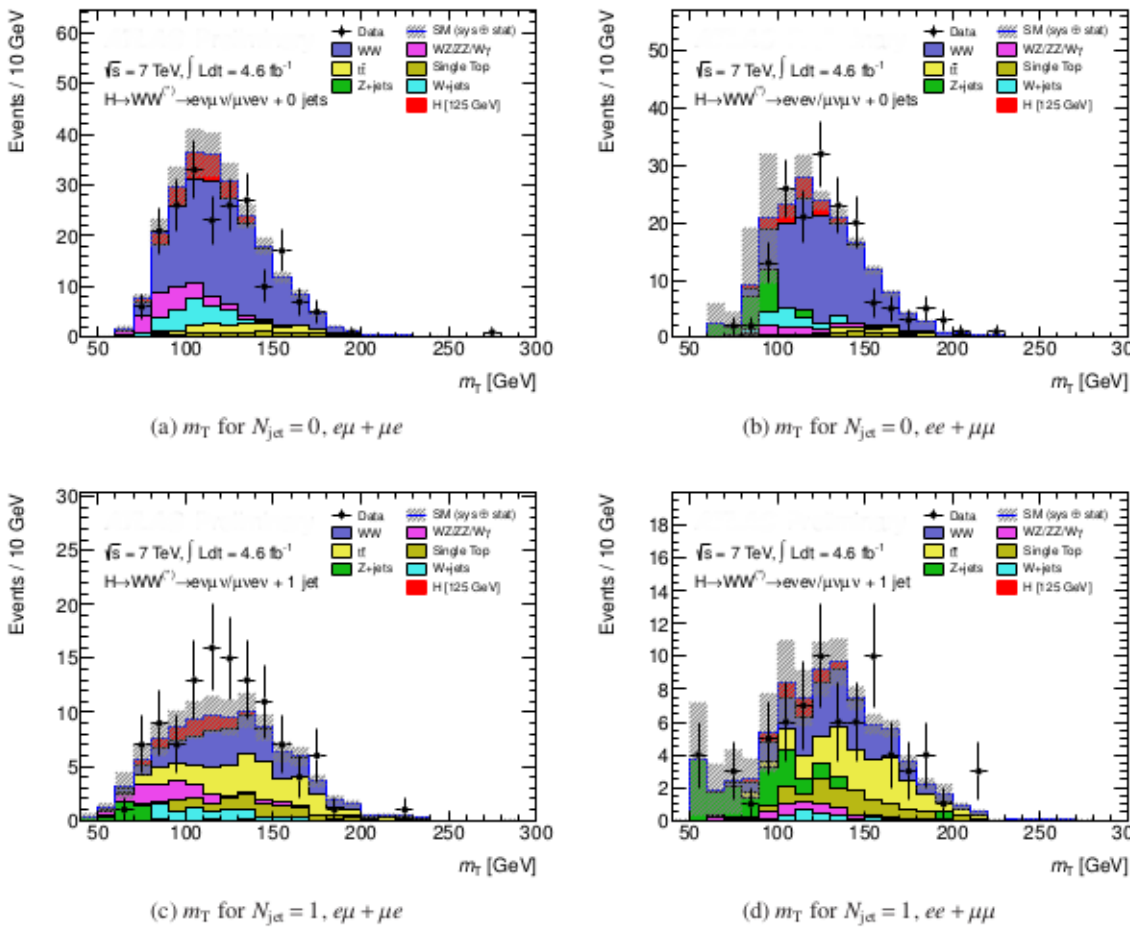

(a) m_{T} for $N_{\text{jet}} = 0$, $e\mu + \mu e$

(b) m_{T} for $N_{\text{jet}} = 0$, $ee + \mu\mu$

(c) m_{T} for $N_{\text{jet}} = 1$, $e\mu + \mu e$

(d) m_{T} for $N_{\text{jet}} = 1$, $ee + \mu\mu$

Figure 5.3: The m_T distribution for the $N_{jet} = 0, 1$ different and same flavor channels for $\sqrt{s} = 8$ TeV.

Chapter 6

Analysis of the Top Background Systematics

An important step in the scientific process is the estimation of errors. Whenever a quantity is measured, there are errors present and in particle physics both systematic and statistical uncertainties exists. The statistical errors arise from the stochastical fluctuations. These types of uncertainties are uncorrelated. Systematic uncertainties on the other hand arise from the measurement apparatus and are usually correlated, one measurement to the next one. Example of sources of systematic uncertainties are the calibration of apparatuses, unknown variable that affects the result, or the probability that an reaction is not detected. These types of uncertainties can shift the expection value of the quantity measured and can therefore lead to a misleading result. The systematic uncertainties can be further divided into experimental and theoretical uncertainties. An example of an experimental uncertainty is in the measurement of the energy of jets. An example of theoretical uncertainties are the neglected contributions from higher order terms in the matrix elements calculations.

In order to get a reliable result, the systematic error need to be taken into account. Most of the time, the estimation of the systematic uncertainties can be treated after they are discovered. The systematic uncertainties are calculated and included in the statistical treatment of the analysis with the other types of uncertainties.

6.1 Top Background Extrapolation

Particle physics events are simulated by event generators that are subject to systematical uncertainties. These uncertainties arise from four different parts of the simulation; QCD scales, parton distribution function (PDF) modelling, matrix element modelling (ME), and parton shower modelling (PS) [29].

6.1.1 QCD Scales

Uncertainties arise in the renormalization and factorization scales because of higher order terms that are not included in the algoritms. To calculate the effects of these, the scales of these are varied in the range 1/2-2 in the simulations. The biggest difference, occuring

because of the variation of the renormalization and factorization scales, in the estimation of the extrapolation factor is used to estimate the uncertainty.

6.1.2 PDF Modelling

The PDF affects the calculations of the cross section for the p-p interaction and it is therefore important to investigate systematic uncertainties in PDF modelling. Since quarks are always bounded in partons, it is necessary to be able to describe the momentum distribution of the quarks inside the parton. This is done by a PDF which is determined from experimental data. The uncertainties in the PDF are calculated by comparing different PDF models.

6.1.3 Matrix Element Modelling

The matrix element, ME, simulates the hard scattering processes. It is needed to calculate the cross section for processes, which is why it is important to study the uncertainties in the modelling of it. The systematic uncertainties are estimated by comparing the samples generated using different ME models.

6.1.4 Parton Shower Modelling

Parton showers, PS, are radiation from QCD processes. The PS models the radiation processes and hadronizations of quarks that occurs after the hard interaction of two partons. The systematic uncertainties are calculated in the same way as for the ME and will be discussed further below.

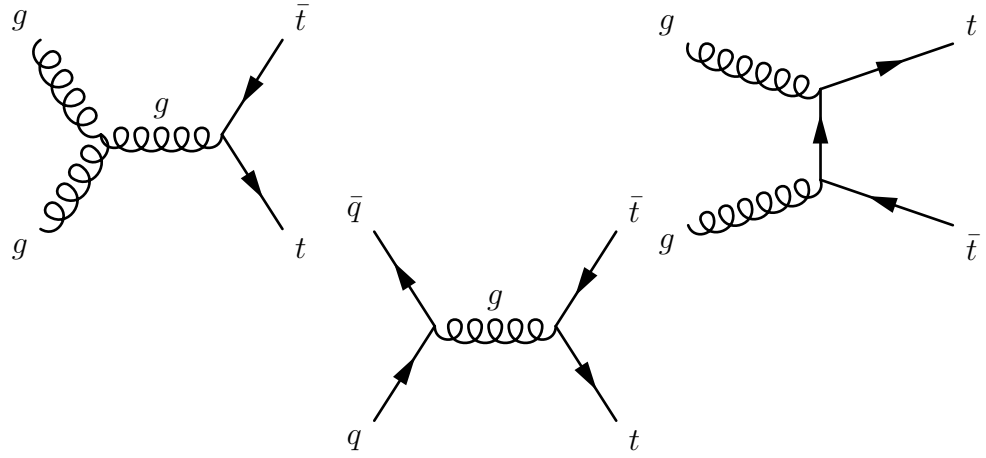

Figure 6.1: The leading order Feynman diagrams for top-quark pair production.

6.2 Top Quark Diagrams

Since the Wt processes contains a real W boson and can decay two charged leptons plus two neutrinos plus one jet (from the b quark), these processes are the largest contribution to the single top background in the 1-jet channel [32]. The t quark decays mainly to

$t \to bW$, and thus contributes significantly to the background in the $H \to WW^* \to \ell\nu\ell\nu$ channel. The processes that contribute to the top background are: $t\bar{t}, Wt, tb, tqb$. The $t\bar{t}$ is called top pair production, while the Wt, tb, tqb are called single top processes. For calculating the uncertainties of the MC generator modelling in the 1-jet channel, the Wt and $t\bar{t}$ were used. The Feynman diagrams for these are shown in Fig. 6.1 and Fig. 6.2 respectively.

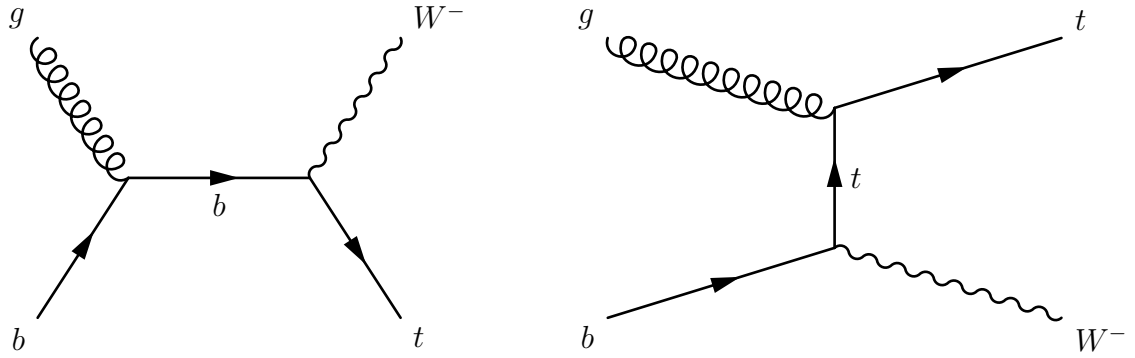

Figure 6.2: The two tree-level Feynman diagram that contributes to the Wt background.

6.3 Uncertainties in Generator Modelling

In this section the estimation of the uncertainties in the parton shower and matrix element modelling are presented. The analysis is done for $H \to WW^* \to \ell\nu\ell\nu$ process for the $N_{jet} = 1$ analysis. The uncertainties are calculated using generator level samples or so called truth samples where no attempt is made to model detector response [29].The calculation is done by exchanging the nominal top background MC samples for samples simulated by generators other than the nominal one and calculate the change in the numerical value for the extrapolation coefficient.

The uncertainties are obtained by first calculating the extrapolation factors defined as

$$\alpha_{SR,DF} = \frac{n_{SR,DF}}{n_{mtW,DF}} \qquad \text{and} \qquad \alpha_{WWCR,DF} = \frac{n_{WWCR,DF}}{n_{mtW,DF}}$$

for different flavor (DF) final states and

$$\alpha_{SR,SF} = \frac{n_{SR,SF}}{n_{mtW,DF}} \qquad \text{and} \qquad \alpha_{WWCR,SF} = \frac{n_{WWCR,SF}}{n_{mtW,DF}}$$

for same flavor (SF) final states. $n_{SR_{DF}}$ and $n_{SR_{SF}}$ are the number of events in the signal region for DF and SF final states resepctively and $n_{mtW_{DF}}$ is the number of events passing the last cut, in this case the transverse mass M_T^W.

6.3.1 MC Samples

The MC samples used for the estimation of the uncertainties are given in Tab. 6.1. The first two samples are the the nominal samples. The default generator for the ME is

Sample ID	Channel	σ [pb]	ME	PS
181087	$t\bar{t}$ (dilepton)	252.89	POWHEG	PYTHIA
110141	Wt (dilepton, DR)	2.349	POWHEG	PYTHIA
110001	$t\bar{t}$ (dilepton)	252.89	MC@NLO	HERWIG
108346	Wt	22.37	MC@NLO	HERWIG
181088	$t\bar{t}$ (dilepton)	252.89	POWHEG	HERWIG
110147	Wt (dilepton, DS)	2.349	POWHEG	HERWIG
110145	Wt (dilepton, DR)	2.349	POWHEG	HERWIG

Table 6.1: Table of the generated samples with their cross sections. The first two samples are the nominal ones, using the default generators for the ME and PS. The rest are the alternative samples.

POWHEG and the default generator for the PS is PYTHIA.

All except the 108346 sample are dilepton filtered meaning that all events that do not contain two leptons are filtered out. This does not affect the analysis in the $H \to WW^* \to \ell\nu\ell\nu$ channel since it is required for an event to have two leptons to pass the selection cuts.

One last thing to note about the samples are the DR and DS samples for the Wt channel. These samples uses either diagram removal (DR) or diagram subtraction (DS) algorithms to remove the overlap between the $t\bar{t}$ and Wt channels. The DR method removes the diagrams that exist in both samples from one of the samples before squaring the amplitude while in the DS method, the diagrams are substracted after the squaring of the amplitude [32].

6.3.2 Estimation of the Uncertainties

It is important to only vary one part of the generator, the ME or PS, at a time since it is assumed that they are uncorrelated. Since the uncertainties calculated are for the top background in the $N_{jet} = 1$ channel the samples are subjected to the selection cuts for that channel. The cutflows for the the different samples are given in the Tab. 6.26.36.46.5. The tables show the number of events passing each selection cut with their statistical uncertainty. Since it it assumed that these processes follow Poisson distribution and that the events are independent of each other, the statistical uncertainty for the number of events, n, passing a selection cut is $\sigma = \sqrt{n}$. The cutflows show only the number of events passing each cut for the DF final state. The number of events in the SR and CR region and the extrapolation factors for SF final states are also given in the cutflows.

The extrapolation factors also have a statistical uncertainty, given by the standard propagation of error [33]:

$$\sigma_\alpha = \sqrt{\sum_i \left(\frac{\partial f}{\partial n_i}\right)^2 \sigma_{n_i}^2}$$

which in this case is given by

$$\sigma_\alpha = \sqrt{\left(\frac{\partial \alpha}{\partial n_{SR}}\sigma_{SR}\right)^2 + \left(\frac{\partial \alpha}{\partial n_{mtW}}\sigma_{mtW}\right)^2} = \sqrt{\left(\frac{1}{n_{mtW}}\sigma_{SR}\right)^2 + \left(\frac{n_{SR}}{n_{mtW}^2}\sigma_{SR}\right)^2}.$$

The statistical uncertainty for the extrapolation factors are also given in the cutflows.

Finally, the uncertainty in the ME and PS generator is given by the relative difference in extrapolation factor for the two generators. For ME (POWHEG+HERWIG vs. MC@NLO+HERWIG) we get

$$\Delta\alpha_{ME} = \frac{\alpha_{MC@NLO} - \alpha_{POWHEG}}{\alpha_{POWHEG}}$$

and for PS (POWHEG+PYTHIA vs. POWHEG+HERWIG) we get

$$\Delta\alpha_{PS} = \frac{\alpha_{HERWIG} - \alpha_{PYTHIA}}{\alpha_{PYTHIA}}.$$

The statistical errors for the relative difference are also given by the propagation of error formula.

6.3.3 Results

The estimation of the systematic uncertainties for the generator modelling in the top background in the $N_{jet} = 1$ $H \to WW^* \to \ell\nu\ell\nu$ channel is given in Tab. 6.6. The relative difference in the extrapolation factors for SR and WWCR are listed in the table. The total uncertainty in the generator modelling, given by the quadrature

$$\Delta\alpha_{tot} = \sqrt{(\Delta\alpha_{ME})^2 + (\Delta\alpha_{PS})^2},$$

and the relative difference between DR and DS are also given in the table. As can be seen, the difference in DR and DS is so small that they are not taken into acount in the calculation of the total uncertainty.

The total theoretical uncertainty on the extrapolation parameters are given by adding the uncertainties in the generator modelling with the PDF and QCD scale uncertainties. Tab. 6.7 [29] lists the uncertainties for all the four parts. The theoretical uncertainties in the extrapolation factors show an reduction of order of three times compared to the previously used values. The reason for this is the use of generator level samples that have high statistics.

6.3.4 Conclusion

The estimation of the uncertainties in the generator modelling for the extrapolation parameters is given in Tab. 6.6 and the estimation of the total theoretical uncertainties in the extrapolation parmeters in Tab. 6.7. The relative difference in the DS and DR is negligible and is not taken into account. As can be seen in Tab. 6.7, the uncertainties in the generator modelling contributes the most to the overall theoretical uncertainty in the extrapolation factors.

These new estimations on the uncertainties are used in the updated analysis of the $H \to WW^* \to \ell\nu\ell\nu$ channel for $N_{jet} = 1$ that is being done on the data taken from 2011 and 2012. The use of the generator level samples have improved the estimations on uncertainties in the extrapolation parameters.

Powheg+Pythia:			
Selection cuts	$t\bar{t}$	Wt	Total top
2 leptons: $p_T^{lead} > 22$ GeV, $p_T^{sublead} > 10$ GeV, $\|\eta_\mu\| < 2.5$, $\|\eta_e\| < 2.47$ (excl. $1.37 < \|\eta_e\| < 1.52$)	3531500 ±1900	35170 ±190	3566700 ±1900
Opposite charge leptons	3100300 ±1800	31750 ±180	3132000 ±1800
Mll > 10 GeV	3007900 ±1700	30980 ±180	3038900 ±1700
$\|m_{ll} - m_Z\| < 15$ GeV	3007900 ±1700	30980±180	3038900 ±1700
MET> 20 GeV	2822500 ±1700	28760 ±170	2851300 ±1700
1 jet	171500 ±400	5600 ±70	177100 ±400
mtWboson > 50 GeV	133900 ±400	4330 ±70	138300 ±400
$m_{\ell\ell} < 55$ GeV	34990 ±190	1120 ±30	36110 ±190
$Z\tau$-Veto	12500 ±400	4000 ±60	129000 ±400
$\Delta\phi_{\ell\ell} < 1.8$	27830 ±170	930 ±30	28760 ±170
DF: nSR	27830 ±170	930 ±30	28760 ±170
DF: nWWCR	59200 ±200	1900 ±40	61100 ±200
SF: nSR	25280 ±160	840 ±30	26120±160
SF: nWWCR	21430 ±150	650 ±30	22080 ±150
α_{SR_DF}	0.2078 ±0.0014	0.214 ±0.008	0.2080 ±0.0014
α_{WWCR_DF}	0.442 ±0.002	0.440 ±0.012	0.442 ±0.002
α_{SR_SF}	0.1888 ±0.0013	0.194 ±0.007	0.1889 ±0.0013
α_{WWCR_SF}	0.1600 ±0.0012	0.151 ±0.006	0.1597 ±0.0012

Table 6.2: Cuflow table for the nominal samples with POWHEG+PYTHIA (ME+PS) generators.

MC@NLO + HERWIG:			
Selection cuts	$t\bar{t}$	Wt	Total top
2 leptons: $p_T^{lead} > 22$ GeV, $p_T^{sublead} > 10$ GeV, $\|\eta_\mu\| < 2.5$, $\|\eta_e\| < 2.47$ (excl. $1.37 < \|\eta_e\| < 1.52$)	1585800 ±1200	32720 ±180	1618500 ±1300
Opposite charge leptons	1463800 ±1200	25020 ±160	1488800 ±1200
Mll > 10 GeV	1435600 ±1200	23840 ±150	1459500 ±1200
$\|m_{ll} - m_Z\| < 15$ GeV	1435600 ±1200	23840±150	1459500 ±1200
MET> 20 GeV	1347200 ±1200	21530 ±150	1368700 ±1200
1 jet	76600 ±300	3340 ±60	80000 ±300
mtWboson > 50 GeV	59700 ±200	2540 ±50	62300 ±300
$m_{\ell\ell} < 55$ GeV	14880 ±120	650 ±30	15540 ±120
$Z\tau$-Veto	55700 ±200	2350 ±50	58000 ±200
$\Delta\phi_{\ell\ell} < 1.8$	11810 ±110	530 ±20	12350 ±110
DF: nSR	11810 ±110	530 ±20	12350 ±110
DF: nWWCR	26560 ±160	1100 ±30	27550 ±170
SF: nSR	10710 ±100	480 ±20	11180 ±110
SF: nWWCR	9550 ±100	370 ±20	9920 ±100
α_{SR_DF}	0.1978 ±0.0020	0.209 ±0.010	0.1983 ±0.0020
α_{WWCR_DF}	0.443 ±0.003	0.431 ±0.016	0.442 ±0.003
α_{SR_SF}	0.1792 ±0.0019	0.188 ±0.009	0.1796 ±0.0018
α_{WWCR_SF}	0.1599 ±0.0018	0.147 ±0.008	0.1594 ±0.0017

Table 6.3: Cuflow table for the nominal samples with MC@NLO+HERWIG (ME+PS) generators.

Powheg+Herwig (DR):			
Selection cuts	$t\bar{t}$	Wt	Total top
2 leptons: $p_T^{lead} > 22$ GeV, $p_T^{sublead} > 10$ GeV, $\|\eta_\mu\| < 2.5$, $\|\eta_e\| < 2.47$ (excl. $1.37 < \|\eta_e\| < 1.52$)	3630700 ±1900	36000 ±190	3666700 ±1900
Opposite charge leptons	3348200 ±1800	34110 ±190	3382300 ±1800
Mll > 10 GeV	3281100 ±1800	33600 ±180	3314700 ±1800
$\|m_{ll} - m_Z\| < 15$ GeV	3281100 ±1800	33600±180	3314700 ±1800
MET> 20 GeV	3077800 ±1800	31170 ±180	3108900 ±1800
1 jet	168700 ±400	6040 ±80	174800 ±400
mtWboson > 50 GeV	131000 ±400	4630 ±70	135600 ±400
$m_{\ell\ell} < 55$GeV	33510 ±180	1170 ±30	34680 ±180
$Z\tau$-Veto	122000 ±300	4280 ±70	126300 ±400
$\Delta\phi_{\ell\ell} < 1.8$	26560 ±160	980 ±30	27530 ±160
DF: nSR	26560 ±160	980 ±30	27530 ±160
DF: nWWCR	56800 ±200	2000 ±40	58800 ±200
SF: nSR	23990 ±150	870 ±30	24860 ±160
SF: nWWCR	20400 ±140	680 ±30	21080 ±150
α_{SR_DF}	0.2028 ±0.0014	0.210 ±0.007	0.2030 ±0.0013
α_{WWCR_DF}	0.434 ±0.002	0.433 ±0.012	0.434 ±0.002
α_{SR_SF}	0.1831 ±0.0013	0.189 ±0.007	0.1833 ±0.0013
α_{WWCR_SF}	0.1558 ±0.0012	0.146 ±0.006	0.1554 ±0.0012

Table 6.4: Cuflow table for the nominal samples with POWHEG+HERWIG (DR) (ME+PS) generators.

Powheg+Herwig (DS):			
Selection cuts	$t\bar{t}$	Wt	Total top
2 leptons: $p_T^{lead} > 22$ GeV, $p_T^{sublead} > 10$ GeV, $\|\eta_\mu\| < 2.5$, $\|\eta_e\| < 2.47$ (excl. $1.37 < \|\eta_e\| < 1.52$)	3630700 ±1900	36280 ±190	3667000 ±1900
Opposite charge leptons	3348200 ±1800	34440 ±190	3382600 ±1800
Mll > 10 GeV	3281100 ±1800	33910 ±180	3315000 ±1800
$\|m_{ll} - m_Z\| < 15$ GeV	3281100 ±1800	33910±180	3315000 ±1800
MET> 20 GeV	3077800 ±1800	31420 ±180	3109200 ±1800
1 jet	168700 ±400	6460 ±80	175200 ±400
mtWboson > 50 GeV	131000 ±400	4950 ±70	135900 ±400
$m_{\ell\ell} < 55$GeV	33510 ±180	1300 ±40	34100 ±190
$Z\tau$-Veto	122000 ±300	4570 ±70	126600 ±400
$\Delta\phi_{\ell\ell} < 1.8$	26560 ±160	1080 ±30	27640 ±170
DF: nSR	26560 ±160	1080 ±30	27640 ±170
DF: nWWCR	56800 ±200	2100 ±50	58900 ±200
SF: nSR	23990 ±150	970 ±30	24960 ±160
SF: nWWCR	20400 ±140	710 ±30	21100 ±150
α_{SR_DF}	0.2028 ±0.0014	0.218 ±0.007	0.2033 ±0.0013
α_{WWCR_DF}	0.434 ±0.002	0.423 ±0.011	0.434 ±0.002
α_{SR_SF}	0.1831 ±0.0013	0.196 ±0.007	0.1836 ±0.0013
α_{WWCR_SF}	0.1558 ±0.0012	0.142 ±0.006	0.1553 ±0.0012

Table 6.5: Cuflow table for the nominal samples with POWHEG+HERWIG (DS) (ME+PS) generators.

Uncertainties	$\Delta\alpha_{SR\_DF}(\%)$	$\Delta\alpha_{WWCR\_DF}(\%)$	$\Delta\alpha_{SR\_SF}(\%)$	$\Delta\alpha_{WWCR\_SF}(\%)$
PS (DR)	2.4 $\pm$0.9	1.8 $\pm$0.7	3.0 $\pm$0.9	2.7 $\pm$1.0
ME (DR)	-2.4 $\pm$1.2	2.0 $\pm$0.9	-2.0 $\pm$1.2	2.5 $\pm$1.3
Total uncertainty: PS + ME (DR)	3.4 $\pm$1.0	2.7 $\pm$0.8	3.6 $\pm$1.0	3.7 $\pm$1.2
DR vs. DS	0.1 $\pm$0.7	0.08 $\pm$0.5	0.2 $\pm$0.7	0.1 $\pm$0.7

Table 6.6: The uncertainties for the ME and PS for SF and DF and SR and WWCR. DR vs. DS is also included in the table.

Uncertainties	$\Delta\alpha_{SR\_DF}(\%)$	$\Delta\alpha_{WWCR\_DF}(\%)$	$\Delta\alpha_{SR\_SF}(\%)$	$\Delta\alpha_{WWCR\_SF}(\%)$
PS	2.4	1.8	3.0	2.7
ME	-2.4	2.0	-2.0	2.5
PDF	-0.12	0.08	-0.12	- 1.2
QCD scale	-1.1	0.6	-1	1.4

Table 6.7: The theoretical uncertainties for the extrapolation parameters arising from PS, ME, PDF and QCD scale.

Chapter 7

Conclusions

The Higgs boson has been the last missing piece in completing the Standard Model of particle physics. Its existence, explaining how fundamental particles gains mass in a gauge invariant way, was confirmed in 2012 by the ATLAS and CMS experiments at CERN in Geneva, Switzerland.

The Higgs boson, that couples to all the massive particles in the SM, has many decay modes. This thesis presents the updated Higgs analysis of the ATLAS experiment for the $H \to WW^* \to \ell\nu\ell\nu$ channel, using 20 fb^{-1} of data at $\sqrt{s} = 8$ TeV and 4.5 fb^{-1} of data at $\sqrt{s} = 7$ TeV. The analysis is separated into jet multiplicity and flavor combination (same or different flavor of the leptons in the final state). The main background for this mode are $W+$ jets, Drell-Yan processes, WW decays, and top quark processes. To separate the signal events from the background events selection cuts are applied.

The updated analysis is still ongoing and the results have not yet been published. Last years results for the signal strength is $\mu = 1.01 \pm 0.31$ with a statistical significance of 3.8 standard deviations at the Higgs mass $m_H = 125$ GeV.

The author's contribution to the analysis is the estimation of the theoretical systematic uncertainties in the matrix element and parton shower generator modelling in the top background in the $N_{jet} = 1$ $H \to WW^* \to \ell\nu\ell\nu$ channel. The estimation is done by using generator level samples with high statistics. Samples of the top background are generated by the nominal and alternative generators and then compared. The total uncertainty (matrix element and parton shower) is then added in quadrature. This is done for both different and same flavor leptons in the final state, for both control region and signal region (the region of phase space where the signal is maximized). The two methods of removing the overlap, diagram removal and diagram substaction, between the Wt and $t\bar{t}$ processes were also compared. The difference is negligible and is not added in to the uncertainty.

The systematic uncertainties in the Monte Carlo generators are then added to the uncertaintes in QCD scales and PDF to get the total theoretical systematic uncertainties for the extrapolation factors.

Acknowledgements

Firstly, I would like to thank my supervisor Jonas Strandberg for the opportunity to do my master's degree project at KTH and for the guidance through the whole process. I would also like to express my very great appreciation to Jelena Jovicevic for helping me and answering all my questions. My grateful thanks to Cecilia Nyström for the discussions on the subject during the project. Finally, I would like to thank my friends and family for their love and support.

List of Figures

List of Tables

Bibliography

[1] Abe, F. *et al.*: "Observation of Top Quark Production in $\bar{p}p$ Collisions with the Collider Detector at Fermilab", *Phys. Rev. Lett.*, Vol. 74, No. 14, April 1995

[2] Abachi, S. *et al.*: "Search for High Mass Top Quark Production in $\bar{p}p$ Collisions at $\sqrt{s} = 1.8$ TeV", *Phys. Rev. Lett.*, Vol. 74, No. 13, March 1995

[3] DONUT Collaboration: "Observation of Tau Neutrino Interactions", *Phys. Lett. B*, Vol. 504, No. 3, April 2001

[4] Dirac, P. A. M.: *"The Quantum Theory of the Emission and Absorption of Radiation"*, Proceedings of the Royal Society of London, Series A, Vol. 114, 1927

[5] 't Hooft, G and Veltman, M: "Regularization and Renormalization of Gauge Fields", *Nucl. Phys. B*, Vol. 44, No. 1, July 1972

[6] Schwinger, J.: "A Theory of the Fundamental Interactions", *Ann. Phys.*, Vol. 2, No. 5, November 1957

[7] Glashow, S.: "Partial-symmetries of Weak Interactions", *Nucl. Phys.*, Vol. 22, No. 4, February 1961

[8] Englert, F. and Brout, R.: "Broken Symmetry and Mass of Gauge Vector Mesons", *Phys. Rev. Lett.*, Vol. 13, No. 9, August 1964

[9] Higgs, P.W.: "Broken Symmetries, Massless Particles and Gauge Fields", *Phys. Lett.*, Vol. 12, No. 2, September 1964

[10] Higgs, P.W.: "Broken Symmetries and the Masses of Gauge Bosons", *Phys. Rev. Lett.*, Vol. 13, No. 16, October 1964

[11] Guralnik, G.S. *et al.*: "Global Conservations and Massless Particles", *Phys. Rev. Lett.*, Vol. 13, No. 20, November 1964

[12] 't Hooft, G: "Renormalizable Lagrangians for Massive Yang-Mills Fields", *Nucl. Phys. B*, Vol. 35, No. 1, December 1971

[13] Griffiths, D.: *"Introduction to Elementary Particles"*, Weinheim: WILEY-VCH Verlag GmbH & Co. KGaA, 2008

[14] Beringer, J. *et al.*: "Review of Particle Physics", *Phys. Rev. D*, Vol. 86, No. 1, July 2012

[15] Cabibbo, N.: "Unitary Symmetry and Leptonic Decays", *Phys. Rev. Lett.*, Vol. 10, No. 12, June 1963

[16] Kobayashi, M. and Maskawa, T.: "CP-Violation in Renormalizable Theory of Weak Interaction", *Progr. Theor. Phys.*, Vol. 49, No. 2, February 1973

[17] Fukuda, Y. *et al.*: "Evidence for Oscillation of Atmospheric Neutrinos", *Phys. Rev. Lett.*, Vol. 81, No. 8, August 1998

[18] Maki, Z. *et al.*: "Remarks on the Unified Model of Elementary Particle", *Progr. Theor. Phys.*, Vol. 28, No. 5, November 1962

[19] Hasert, F.J. *et al.*: "Search for Elastic Muon-neutrino Electron Scattering", *Physics Letters*, Vol. 46B, No. 1, September 1973

[20] Goldstone, J. *et al.*:"Broken Symmetries", *Phys. Rev.*, Vol. 127, No. 3, August 1962

[21] The ATLAS Collaboration: "The ATLAS Experiment at the CERN Large Hadron Collider", *J. Intstrum.*, Vol. 3, August 2008

[22] Evans, L. and Bryant, P.: "LHC Machine", *J. Instrum.*, Vol. 3, August 2008

[23] The LHC Cross Section Working Group, *et al.*:"Handbook of LHC Higgs Cross Sections: 3. Higgs Properties", CERN-2013-004, July 2013

[24] Denner, A. *et al.*: "Standard Model Higgs-Boson Branching Ratios with Uncertainties", arXiv:1107.5909v2, July 2011

[25] The ATLAS Collaboration: "Observation of a New Particle in the Search for the Standard Model Higgs Boson with the ATLAS Detector at the LHC", *Phys. Lett. B*, Vol. 716, No. 1, September 2012

[26] The CMS Collaboration: "Observation of a New Boson at a Mass of 125 GeV with the CMS Experiment at the LHC", *Phys. Lett. B*, Vol. 716, No. 1, September 2012

[27] The ATLAS collaboration: "Analysis of $H \to WW^* \to \ell\nu\ell\nu$ ggF VBF Production Modes with 20 fb^{-1} and 4.5 fb^{-1} of Data Collected with the ATLAS Detector at $\sqrt{s} = 8$ and 7 TeV,", ATL-COM-PHYS-2014-466, June 2014

[28] The HWW Working Group: "Background Estimates in the $H \to WW^* \to \ell\nu\ell\nu$ Analysis with 20 fb^{-1} of Data Collected with the ATLAS Detector at $\sqrt{s} = 8$ TeV", ATL-COM-PHYS-2013-1630, April 2014

[29] Alison, J. *et al.*: "Theoretical Studies of $H \to WW$ Search and Measurement", ATL-COM-Phys-2013-1541, June 2014

[30] Ranucci, G.: " The Profile Likelihood Ratio and the Look Elsewhere Effect in High Energy Physics", *Nucl. Instr. Meth. Phys. Res. A*, Vol. 661, No. 1, January 2012

[31] The ATLAS Collaboration: "Measurements of the Properties of the Higgs-like Boson in the $WW^* \to \ell\nu\ell\nu$ Decay Channel with the ATLAS Detecor Using 25 fb^{-1} of Proton-Proton Collision Data", ATLAS-CONF-2013-030, Mars 2013

[32] Re, E.: "Single-top Wt-channel Production Matched with Parton Showers Using the POWHEG Method", *Eur.Phys.J.*,Vol. 71, No. 1547, February 2011

[33] Tellinghuisen, J.: "Statistical Error Propagation"; *J. Phys. Chem. A*, Vol. 105, No. 15, February 2001